

UKAEA-CCFE-PR(18)32

B. J. Ding, P. T. Bonoli, A. Tuccillo, M. Goniche, K. Kirov, M. Li, Y. Li, R. Cesario, Y. Peysson, A. Ekedahl, L. Amicucci, S. Baek, I. Faust, R. Parker, S. Shiraiwa, G. M. Wallace, A. Cardinali, C. Castaldo, S. Ceccuzzi, J. Mailloux, F. Napoli, F. Liu, B. Wan and JET Contributors

Review of recent experimental and modeling advances in the understanding of lower hybrid current drive in ITER-relevant regimes

Enquiries about copyright and reproduction should in the first instance be addressed to the UKAEA Publications Officer, Culham Science Centre, Building K1/0/83 Abingdon, Oxfordshire, OX14 3DB, UK. The United Kingdom Atomic Energy Authority is the copyright holder.

Review of recent experimental and modeling advances in the understanding of lower hybrid current drive in ITER-relevant regimes

B. J. Ding,¹ P. T. Bonoli,² A. Tuccillo,³ M. Goniche,⁴ K. Kirov,⁵ M. Li,¹
Y. Li,¹ R. Cesario,³ Y. Peysson,⁴ A. Ekedahl,⁴ L. Amicucci,³ S. Baek,²
I. Faust,² R. Parker,² S. Shiraiwa,² G. M. Wallace,² A. Cardinali,³
C. Castaldo,³ S. Ceccuzzi,³ J. Mailloux,⁵ F. Napoli,³ F. Liu,¹
B. Wan¹ and JET Contributors⁷

¹*Institute of Plasma Physics, Chinese Academy of Science, Hefei 230031, P R China*

²*MIT Plasma Science and Fusion Center, Cambridge, Massachusetts 02139, USA*

³*ENEA, FSN Department, C. R. Frascati, via E. Fermi 45, 00044 Frascati (Roma), Italy*

⁴*CEA, IRFM, F-13108, St-Paul-Lez-Durance, France*

⁵*UKAEA-CCFE, Culham Science Centre, Abingdon, Oxon, OX14 3DB, UK*

⁶*IPP, Boltzmannstrasse 2, 85748 Garching bei München, Germany*

⁷*EUROfusion Consortium, JET, Culham Science Centre, Abingdon, OX14 3DB, UK*

Review of recent experimental and modeling advances in the understanding of lower hybrid current drive in ITER-relevant regimes

B. J. Ding¹), P. T. Bonoli²), A. Tuccillo³), M. Goniche⁴), K. Kirov⁵), M. Li¹), Y. Li¹), R. Cesario³), Y. Peysson⁴), A. Ekedahl⁴), L. Amicucci³), S. Baek²), I. Faust²), R. Parker²), S. Shiraiwa²), G. M. Wallace²), A. Cardinali³), C. Castaldo³), S. Ceccuzzi³) J. Mailloux⁵), F. Napoli³), F. Liu¹), B. Wan¹), JET Contributors⁷)

1) Institute of Plasma Physics, Chinese Academy of Science, Hefei 230031, P R China

2) MIT Plasma Science and Fusion Center, Cambridge, Massachusetts 02139, USA

3) ENEA, FSN Department, C. R. Frascati, via E. Fermi 45, 00044 Frascati (Roma), Italy

4) CEA, IRFM, F-13108, St-Paul-Lez-Durance, France

5) UKAEA-CCFE, Culham Science Centre, Abingdon, Oxon, OX14 3DB, UK

6) IPP, Boltzmannstrasse 2, 85748 Garching bei München, Germany

7) EUROfusion Consortium, JET, Culham Science Centre, Abingdon, OX14 3DB, UK

Email: bjding@ipp.ac.cn, bonoli@psfc.edu.cn

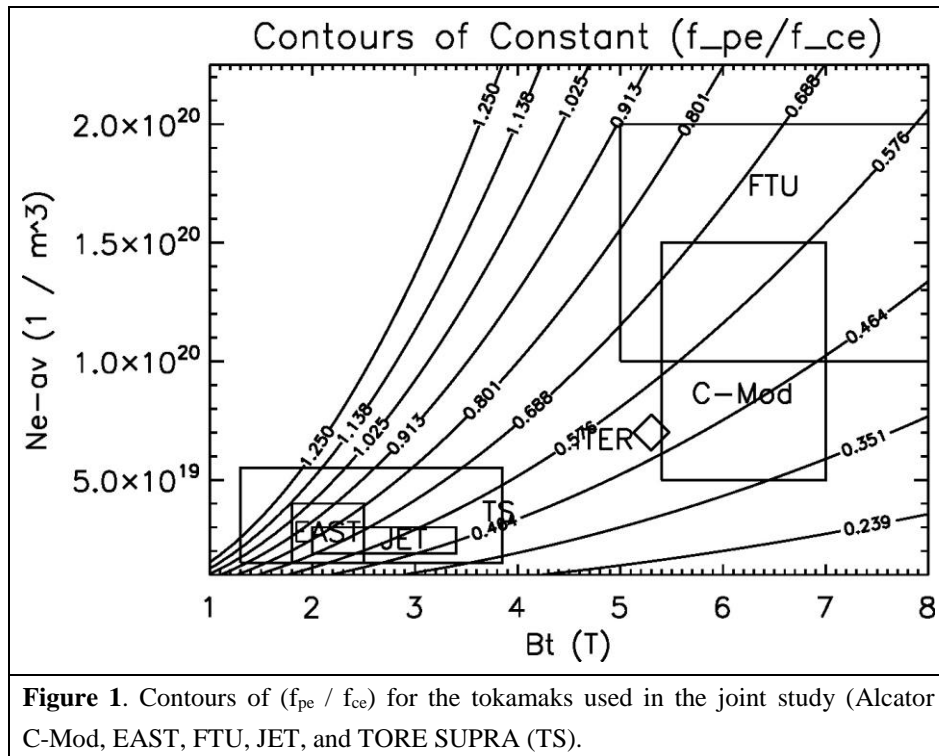
Abstract Progress in understanding lower hybrid current drive (LHCD) at high density has been made through experiments and modeling, which is encouraging given the need for an efficient off-axis current profile control technique in burning plasma. By reducing the wall recycling of neutrals, the edge temperature is increased and the effect of parametric instability (PI) and collisional absorption (CA) is reduced, which is beneficial for increasing the current drive (CD) efficiency. Strong single pass absorption is preferred to prevent CA and high LH operating frequency is essential for wave propagation to the core region at high density, presumably to mitigate the effect of PI. The dimensionless parameter that characterizes LH wave accessibility and wave refraction for the experiments in this joint study is shown to bracket the region in parameter space where ITER LHCD experiments will operate in the steady state scenario phase. Further joint experiments and cross modeling are necessary to understand the LHCD physics in weak damping regimes which would increase confidence in predictions for ITER where the absorption is expected to be strong.

1. Introduction

Lower hybrid current drive (LHCD) has the attractive property of high off-axis ($r/a \approx 0.7$) [1] current drive efficiency making this a useful technique for broadening the current density profile in order to create non-monotonic (shear reversed) profiles of the safety factor – $q(r)$ with $q_{\min} > 2$ and large shear reversal radius ($r/a \approx 0.7$). Moreover, in H-mode regimes, the onset of instabilities characteristic of the pedestal radial layer (at $r/a \approx 0.9$) would be prevented by the natural current profiles produced by bootstrap effect, which can be efficiently matched by LHCD [2][3]. This feature would allow exploiting a high fraction of bootstrap current (≈ 60 -70%), an important condition for viability of an economic fusion reactor [4]. The LHCD tool should be thus considered for the steady state Scenario-4 in the ITER device[5], and for pulsed reactor regimes as well [6][7]. However, how to improve LHCD capability at high density is an important issue to be solved before this application, which is mainly affected by collisional damping losses when the single pass damping is low,

parametric instability (PI), scattering by density fluctuations (SDF), and LH wave accessibility.

In order to investigate physics issues critical for LHCD at reactor relevant densities, a multi-machine assessment, including experiments and modeling in Alcator C-Mod, EAST, FTU, JET, and Tore Supra (TS) tokamaks, has been continued as a joint activity under the coordination of the Integrated Operation Scenarios (IOS) Topical Group of the ITPA. In these joint experiments the C-Mod and FTU tokamaks are operated at high field magnetic field (5-8 T) and high density ($5\text{-}20 \times 10^{19} \text{m}^{-3}$), and EAST, JET and TS are operated (for these experiments) at low to medium field (1.8 – 3.8 T) and lower density ($2\text{-}4 \times 10^{19} \text{m}^{-3}$). Although these LHCD experiments span more than an order of magnitude in density, about a factor of five in toroidal magnetic field, and correspond to both limited (FTU, TS) and diverted (C-Mod, EAST, JET) discharges, their LHCD parameter regimes can be usefully characterized in terms of electron plasma frequency (f_{pe}) to electron gyrofrequency (f_{ce}) ratio (f_{pe}/f_{ce}) (see Fig. 1), which is the fundamental dimensionless parameter that determines wave accessibility, wave penetration, and wave refraction. Note that for these experiments (f_{pe}/f_{ce}) covers a range from 0.35 to ≥ 1.0 which easily brackets the value of 0.5-0.6 expected in the ITER steady state Scenario 4, thus giving some confidence in the extrapolation of results found in these experiments to ITER. In fact, the contour for $(f_{pe}/f_{ce}) \approx 0.48$ passes through the operating space of all five devices. In terms of absolute parameters, the C-Mod, EAST, and FTU tokamaks operate with LH source frequencies of 4.6 – 8.0 GHz, which brackets the source frequency of 5.0 GHz that was planned for ITER. Similarly, both C-Mod and FTU operate at densities of $0.5 - 2.0 \times 10^{20} \text{m}^{-3}$ and magnetic fields (5 – 8 T) which bracket the values of $\sim 0.7 \times 10^{20} \text{m}^{-3}$ and 5.3 T respectively which are anticipated for the ITER Steady State Scenario 4 [5].



Experiments on FTU identified a new method that enabled LHCD at densities comparable to DEMO [8]. This method was assessed on the basis of previous theoretical predictions of diminished parasitic effect of spectral broadening due to PI under higher temperature of plasma edge [9]. In further studies, collisional absorption (CA) [10], and SDF [11][12], individually or in combination, were also proposed as possible candidates for the current drive (CD) efficiency decreasing at high density faster than standard theory prediction [13]. Though studies show that SDF and PI can both broaden the initial N_{\parallel} spectra and affect the CD capability, the mechanisms seem to be essential in terms of achieving agreement between theory and experiment.

The EAST tokamak has both 2.45 GHz and 4.6 GHz LH source power installed which offers the unique capability to study LHCD physics with two different source frequencies applied simultaneously or separately in the same machine. Thus, this manuscript reports also on CD efficiency scaling with source frequency in EAST at fixed density. Lower hybrid current drive experiments performed on the EAST, C-Mod, and FTU devices are typically in the weak damping regime where the injected phase speed is much larger than the phase speed where strong electron Landau damping occurs, i. e. $v_{\parallel} / v_{te} \gg 2.5$, where $v_{te} = (2T_e / m_e)^{0.5}$. In these experiments, interaction of the LH wave with the cold scrape off layer occurs which can lead to parasitic absorption of the wave power in the edge. The EAST device has the capability to study LHCD physics in this weak damping regime with different edge conditioning techniques such as Supersonic Molecular Beam Injection (SMBI), weak lithiation, and strong lithiation, thus testing the effectiveness of these different techniques for mitigating parasitic losses in the SOL.

The Alcator C-Mod tokamak is operated under a wide range of densities and magnetic field which make it possible to study LH current drive at the actual absolute values of density and magnetic field anticipated for ITER. Control of the SOL width in C-Mod by increasing the plasma current make it possible to study and mitigate parasitic interactions of the LH wave with the SOL due to PI and CA [14].

Finally the JET tokamak with its significant auxiliary heating power in the form of Neutral Beam Injection (NBI) makes it possible to study far off-axis LHRF power deposition and current generation, which is the ultimate application goal for LHCD in a reactor grade plasma.

As part of these studies computational models for linear and nonlinear wave propagation and absorption are necessary to interpret and analyze experimental results. In order to more accurately capture parasitic interactions of the LH wave with the SOL due to CA we have implemented realistic plasma profiles and SOL geometry in an advanced ray tracing / Fokker Planck code. In addition the effect of SDF has been included in these models viz. spectral broadening of the power spectrum [15] coupled from the LH waveguide launcher. The importance of edge density profiles in determining the coupled LH launcher spectra [16] has also been investigated and found to be important. Finally an improved parametric dispersion code was used to study nonlinear excitation of the LH wave (sideband) in the parallel coupling limit. In this case the excited sideband LH wave spends longer time at the plasma edge where it is unstable to parametric instabilities.

The manuscript is arranged as follows. In section 2, results from the joint experimental activity are presented, followed by the cross-study and data analysis in section 3. Finally, conclusions and discussion will be given in section 4.

2. Results from joint experimental activity

2.1 EAST

EAST experiments aim at fully assessing conditions useful for enabling the LHCD effect into a dense plasma core. As shown in Fig. 2, first LHCD results [17] with 4.6GHz show that the lower hybrid wave (LHW) can be coupled to plasma with low reflection coefficient, drive plasma current and plasma rotation, modify the plasma current profile, and heat the plasma efficiently. Meanwhile, good plasma heating is observed with core electron temperature above 4 keV [17].

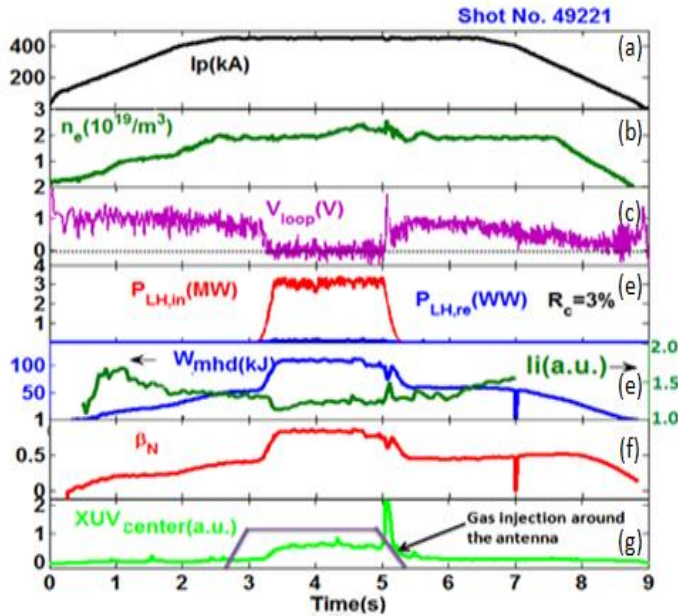


Figure 2. Typical waveforms of coupling, current drive and plasma heating in EAST for 4.6GHz LH power injection. (a) Plasma current (kA) vs time (s), (b) line averaged density (10^{19} m^{-3}) vs time (s), (c) loop voltage (V) vs time (s), (d) Injected LH power (MW) in red and reflected LH power (MW) in blue vs time (s), (e) Stored energy (kJ) in blue and internal inductance (green) vs time (s), (f) $\beta_N = \beta_t / [I_p(\text{A}) / (a(\text{m}) / B(\text{T}))]$ vs time (s), (g) XUV (a. u.) at the center (green) and gas injection at the antenna (a. u.) in black vs time (s). Figure reproduced from Ref. [17].

The effect of lower hybrid (LH) frequency, with $N_{\parallel}^{\text{peak}}=2.1$ for 2.45GHz and $N_{\parallel}^{\text{peak}}=2.04$ for 4.6GHz, on LHCD characteristics at $n_e = 2.0 \times 10^{19} \text{ m}^{-3}$ with the same coupled power (1.05MW) in a lower single null (LSN) configuration was investigated in EAST (see Fig. 3)[18][19]. Here, N_{\parallel} is the refractive index parallel to the applied magnetic field and $N_{\parallel}^{\text{peak}}$ is the peak value. It shows the residual voltages (V_{loop}) are 0.27V and 0.15V, respectively, during 2.45 GHz and 4.6 GHz application, possibly implying a higher CD efficiency for the 4.6 GHz LH system. Better plasma heating effect for 4.6 GHz can be seen from the time evolution of plasma stored energy, and central electron temperature (T_{e0}) measured with an X-ray Crystal Spectrometer (XCS) [20]. The internal inductance (l_i) is higher with the 4.6GHz LH wave injection, meaning a more peaked current profile. The plasma rotation shows, for similar power input, a larger central rotation change with 4.6GHz. The increase of heat load on the divertor inferred from the temperature measurement with the infra-red camera combined with the increase of the stored energy W_{dia} suggests an increase of the LHCD power absorbed by the plasma for the 4.6GHz antenna.

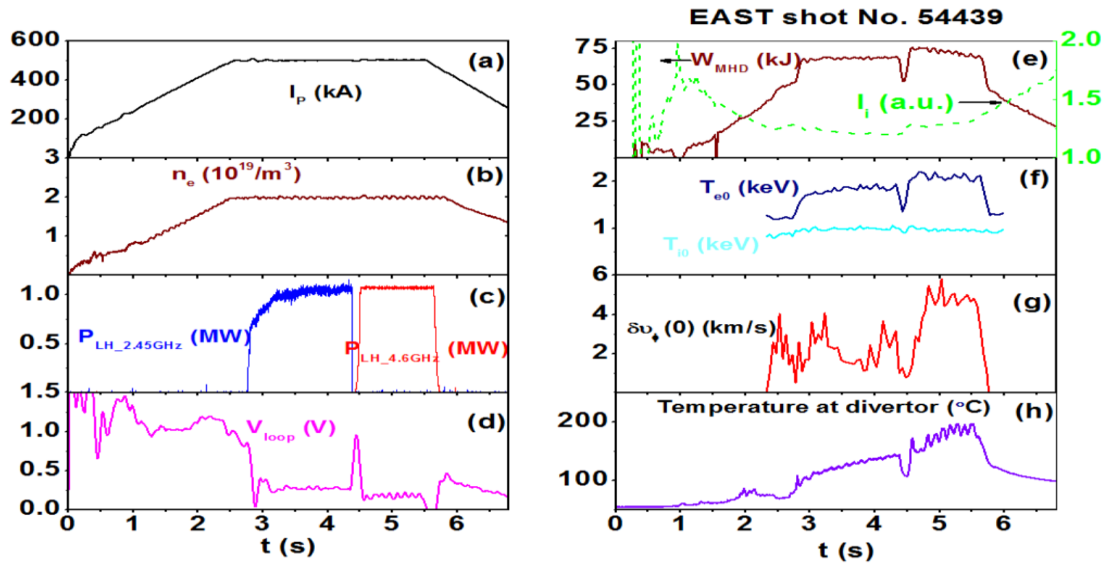


Figure 3. Typical waveform of LH frequency effect on plasma characteristics in the EAST Tokamak. (a) Plasma current (kA) vs time (s), (b) line averaged density (10^{19} m^{-3}) vs time (s), (c) LH power (MW) at 2.45 GHz in blue and LH power (MW) in red at 4.6 GHz vs time (s), (d) Loop voltage (V) vs time (s), (e) Stored energy (kJ) in brown and internal inductance (a. u.) in green vs time (s), (f) Central electron temperature (keV) in blue and central ion temperature (keV) in cyan vs time (s), Central rotation velocity (km/s) vs time (s), and (h) Temperature at divertor ($^{\circ}\text{C}$) vs time (s).

These experimental results demonstrate that LHWs at 4.6 GHz exhibit stronger CD effect than at 2.45 GHz, which is consistent with less pronounced PI behavior with 4.6 GHz LH wave (see Fig. 4). However, this difference can also be attributed to a reduction in the power of the main forward lobe at 2.45 GHz relative to 4.6 GHz because of large reflection coefficients ($\approx 10\%$) in the 2.45 GHz system [as to be discussed further in Sec. 3.4 (b)].

By means of simultaneous injection of 4.6 GHz and 2.45 GHz LH power, as shown in Fig. 5, H-mode is obtained in EAST at relatively high density, even up to $n_e \sim 4.5 \times 10^{19} \text{ m}^{-3}$, where a current drive effect is still observed, as indicated by the trace for electron cyclotron emission (ECE) located at the major radius of 2.33m. In this case the higher toroidal magnetic field at the geometric center ($R=R_0$), $B_0 = 2.8 \text{ T}$, improves LH wave accessibility for both frequency sources, thus making it possible to penetrate to the higher densities. In particular note from Fig. 5 the initial loop voltage drop to $V_{\text{Loop}} \approx 0.35 \text{ V}$ that occurs with application of 2.45 GHz LH power is maintained as the line averaged density continues to ramp up from $\sim 1.5 \times 10^{19} \text{ m}^{-3}$ to $4.5 \times 10^{19} \text{ m}^{-3}$ via application of the 4.6 GHz LH power.

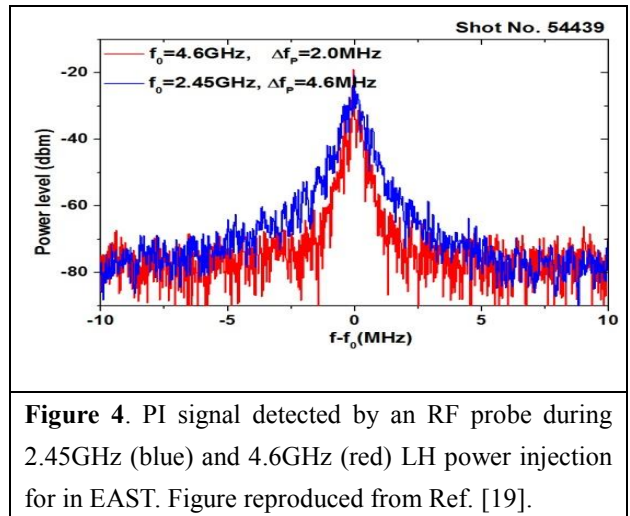


Figure 4. PI signal detected by an RF probe during 2.45GHz (blue) and 4.6GHz (red) LH power injection for in EAST. Figure reproduced from Ref. [19].

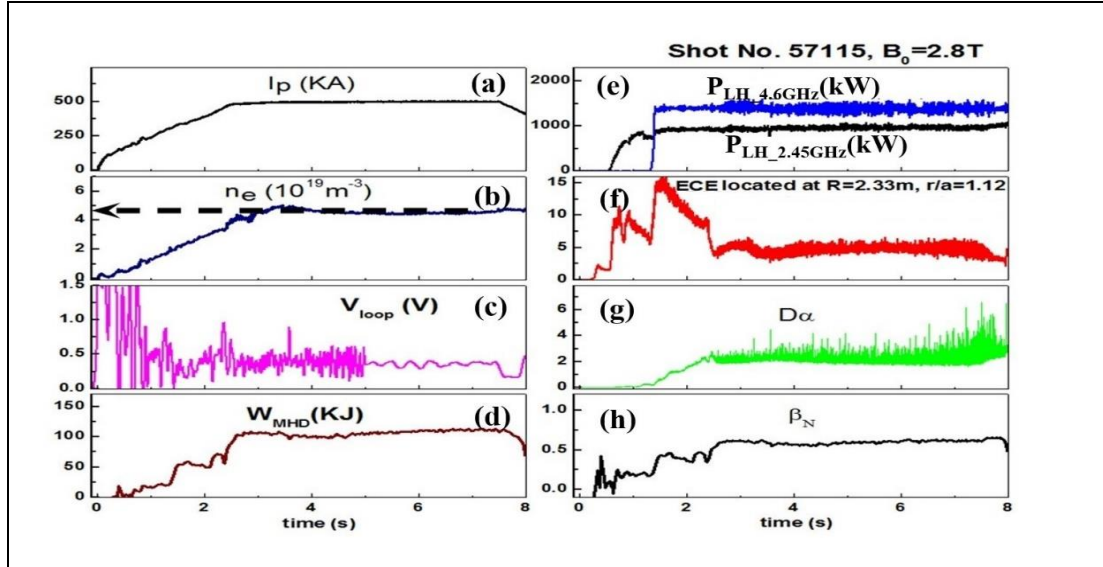


Figure 5. H-mode achieved with LHCD at high density in the EAST tokamak. (a) Plasma current (kA) vs time (s), (b) line averaged density (10^{19} m^{-3}) vs time (s), (c) Loop voltage (V) vs time (s), (d) Plasma stored energy (kJ) vs time (s), (e) 2.45 GHz LH power (MW) in black and 4.6 GHz power in blue vs time (s), (f) Electron cyclotron emission (ECE) vs. time (s), (g) D-alpha emission vs time (s), and (h) $\beta_N = \beta_t / [I_p(\text{A}) / (a(\text{m}) / B(\text{T})]$ vs time (s). Figure reproduced from Ref. [19].

However, a transport analysis including LH current drive sources would be needed in order to separate the contribution of heating and non-inductive current drive to the loop voltage drop. One can gain insight into the effect of PI in the discharge shown in Fig. 5 by examining the behavior of the ECE as a function of density (see Fig. 6). Referring to Fig. 6 it can be seen that a weak power law is found ranging between n_e^{-1} and $n_e^{-1.5}$, suggesting a negligible behavior or weak effect from PI for the density range $(1.5\text{-}5.0) \times 10^{19} \text{ m}^{-3}$ with the 4.6 GHz launcher.

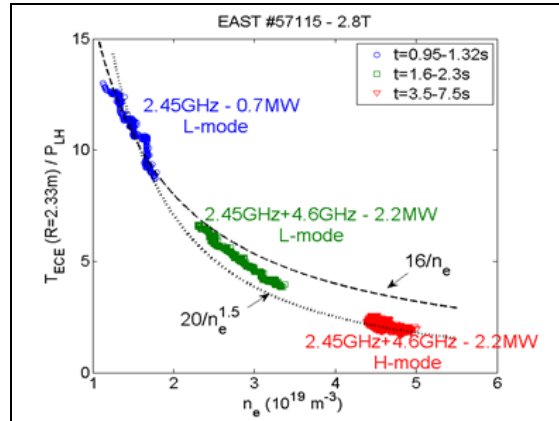


Figure 6. Electron cyclotron emission (ECE) vs. line-averaged electron density for EAST discharge.

2.2 Alcator C-Mod

On Alcator C-Mod, the LH RF physics program focuses on improving the current drive at high density and understanding how to properly extrapolate present experiments to a reactor. The power deposition of LH RF waves into the edge plasma of a diverted tokamak has been systematically measured for the first time in the experiment. By means of fast time resolution edge diagnostic sets including innovative fast-thermocouples, an extensive set of Langmuir probes, and a Ly-alpha ionization camera, LH power modulation reveals that the LH power is deposited very close to or outside of the LCFS. The loss of current drive at high density correlates with the existence of a cold, dense and highly collisional divertor plasma [21].

In a reactor, LH waves will experience strong single pass absorption, and therefore, the direct interaction with cold dense regions of the scrape-off-layer discussed above can be minimized naturally. However, LH waves still must propagate a significant length in the poloidal/toroidal directions through the SOL plasmas before crossing the last closed flux surface. A suite of new diagnostics was installed in C-Mod to better characterize the LH wave propagation during this first pass from the launcher to core. Two sets of RF magnetic probe arrays were installed at different toroidal locations which are magnetically mapped to the launcher.

Figure 7 shows the LH wave power as a function of density measured by one of new RF probe arrays [14]. A reduction of LH power at the launched frequency (4.6 GHz) is observed in all three discharges with different plasma currents. The highest current case shows smaller reduction of LH power compared to other two. This trend is consistent with the recovery of current drive at high current [22][23], suggesting that significant modification of the wave spectrum occurs during the first pass and may be responsible for the loss of current drive. As the current is increased, the SOL width is measured to decrease significantly, placing the LH slow wave cut-off closer to the last closed flux surface (LCFS). This is consistent with reduced parasitic losses in the SOL via collisional absorption (a reduction in the mean collisionality of plasma in the SOL) and parametric instability, since now the distance transited by the LH wave between the cut-off and LCFS is reduced. Figure 7 also shows the signal strength at 4.57 GHz, indicating the spectrum power in this frequency range increases to about 10 dB below the peak power as the density increases. Note that the 4.57 GHz

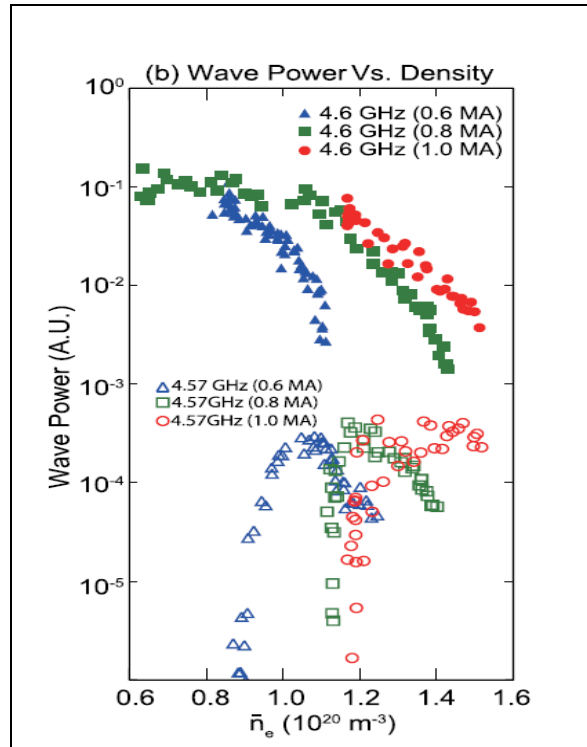


Figure 7. Wave power measured with the three probe array as a function of the line-averaged density at three different plasma currents in Alcator C-Mod. Blue triangles, green squares, and red circles correspond respectively to 0.6 MA, 0.8 MA, and 1.0 MA discharges Figure reproduced from Ref. [14].

data shown in the figure corresponds to the ion-cyclotron PI sideband LH waves. In contrast to ion-sound PI's, which are stabilized with collisional absorption [24], those decay waves corresponding to the ion-cyclotron side bands remain unstable for a wide range of edge parameters found in various tokamaks and can be responsible for increased parasitic power losses universally observed in various LH experiments.

2.3 JET

On JET, as shown in Fig. 8, for plasmas in weakly accessible conditions, the fast electron tail decays, as it does on Tore Supra when the density is normalized to $n_{e\text{-accessibility}}$. However the role of LH wave accessibility is difficult to assess in Fig. 8. For example, when comparing

the HXR data of EAST ('poor lithium' case) with 2.45GHz system to the ECE data of JET a similar decay of the fast electron tail is observed for $n_e > 2 \times 10^{19} \text{m}^{-3}$ although the LH waves could penetrate deeper in the EAST plasma [25]. Thus LH wave accessibility would not necessarily play a significant role in those discharges as indicated by similar behavior of fast electron data in inaccessible/accessible conditions [26][27]. As will be discussed in Section 3.4, recent time dependent ray tracing / Fokker Planck analysis [28] has indicated that loss of wave accessibility at high density in JET could be partially responsible for a reduction in the LHCD effect. However this analysis relies on multiple passes of the LH wavefront between the slow wave cut-off and the confluence layer between the slow and fast wave modes in plasma. On the other hand, detailed analysis of spectral broadening via the PI effect has shown that this mechanism is a strong candidate for the decrease in HXR emission since the density at large radii in these discharges exceeds a critical value of $\approx 4 \times 10^{19} \text{m}^{-3}$, which promotes conditions of cold plasma edge that favours the undesired effect of PI spectral broadening [8][26]. Furthermore the experimental interpretation in terms of the PI effect can be understood in terms of a relatively straightforward single pass damping analysis.

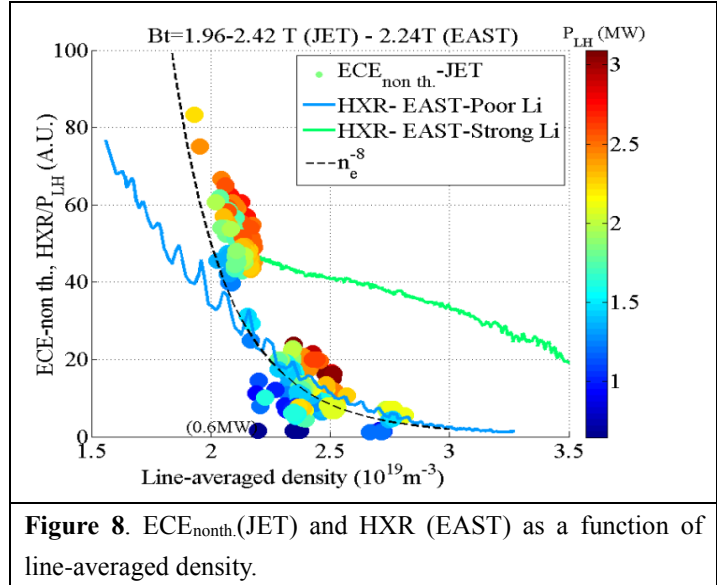


Figure 8. ECE_{nonth.}(JET) and HXR (EAST) as a function of line-averaged density.

3. Cross-study and data analysis

In this section we present modelling results for LHCD in C-Mod, EAST, and JET in order to assess the roles of LH wave accessibility, parametric instability, collisional absorption, and scattering by density fluctuations in determining wave absorption in these experiments as well as the larger decrease of CD efficiency than predicted by theory at high density [29]. In Section 3.1 it will be shown through ray tracing / Fokker Planck analysis of discharges in C-Mod and EAST that spectral broadening of the initial LH launcher spectrum (via processes such as PI and SDF) can be invoked in order to obtain profiles of LHRF power deposition, LH current density, and hard x-ray emission that are consistent with experimental measurements in these devices. In Section 3.2 ray tracing /Fokker Planck results are shown for Alcator C-Mod which demonstrates that collisional absorption of LH waves in the SOL can explain the reduction in hard x-ray emission as the density is increased. In Section 3.3 a new ray tracing / Fokker Planck model is applied to LHCD in JET where the role of LH wave accessibility at high density is assessed. Finally in Section 3.4, analysis results are presented to interpret the differences seen in the LHCD efficiency with 2.45 GHz and 4.6 GHz LH power in EAST. In Section 3.4 (a) it is shown that suppression of PI at higher LH source frequency is also consistent with experimental results in the EAST experiments. Sections 3.4 (b) – 3.4(c) assesses these experiments using ray tracing / Fokker Planck treatments combined

with a careful accounting for the coupled power spectrum from each frequency launcher. Section 3.4(d) concludes with a discussion of the difficulties associated with accounting for the DC electric field in these two-frequency discharges.

3.1 Role of spectral broadening in LHCD experiments in C-Mod and EAST

Measurements indicate there is little change in the LH power density profile in the density range where good current drive is obtained. Furthermore, the simulated profiles of driven current density, power deposition, and hard x-ray emission do not always agree with experimental measurements in Alcator C-Mod [35] and Tore Supra [36], with the simulated profiles being off-axis and hollow compared to those in the experiment. The existence of a “tail” in the launched power spectrum due to SDF [15], considered in C3PO/LUKE codes [37][38], greatly reduces model sensitivity to plasma conditions while at the same time significantly improves the consistency between modeling and experiments in plasma conditions for which the spectral gap is large in EAST and Alcator C-Mod [39], as well as in the Tore Supra tokamak (see Fig. 9). The spectral modifications employed in C3PO / LUKE typically place $\leq 50\%$ of the incident LH power in a “tail” that extends from $2 \leq N_{\parallel} \leq 5$ and that is modeled by a series of smaller Gaussian power lobes.

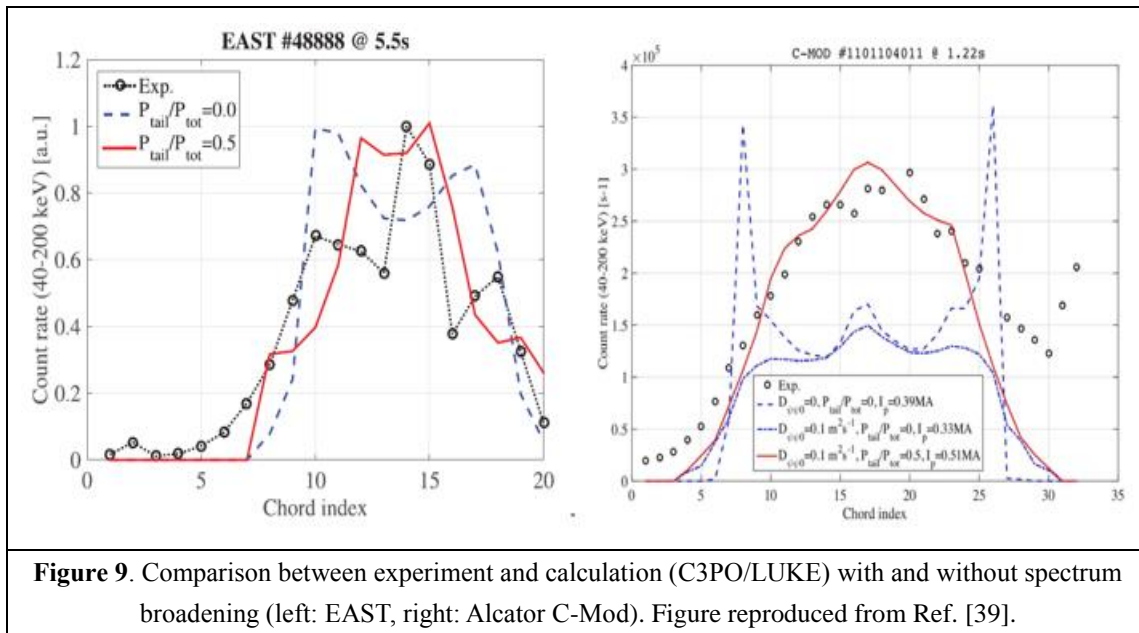


Figure 9. Comparison between experiment and calculation (C3PO/LUKE) with and without spectrum broadening (left: EAST, right: Alcator C-Mod). Figure reproduced from Ref. [39].

The “tail” model employed in GENRAY / CQL3D[40][41] places 5-10% of the incident LH power in smaller Gaussian power lobes at $N_{\parallel} \approx 2.5-2.7$. An example using GENRAY/CQL3D for the EAST tokamak is shown in Fig. 10, where a relocation of 10% of total LH power to modestly high N_{\parallel} (~ 2.7) gives the best fit to the experimental HXR emission profile shape. At this time the differences needed in the spectral broadening in C3PO/LUKE and GENRAY/CQL3D in order to improve agreement with experiment are under study.

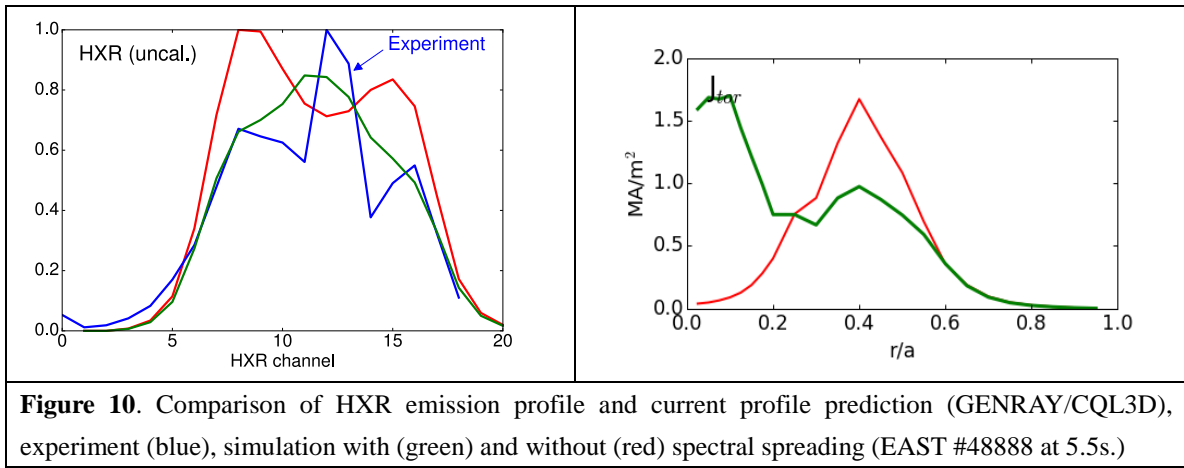


Figure 10. Comparison of HXR emission profile and current profile prediction (GENRAY/CQL3D), experiment (blue), simulation with (green) and without (red) spectral spreading (EAST #48888 at 5.5s.)

3.2 Role of collisional absorption in the Alcator C-Mod density limit

Simulations of CA using GENRAY/CQL3D suggest that SOL plasmas can have significant impact on current drive when single pass absorption is weak. Recently a model which takes into account realistic SOL geometry and the existence of a cold dense plasma near the divertor was implemented in GENRAY. Previously when the computation domain of GENRAY had been extended to include SOL plasmas, the SOL plasma density and temperature profiles were assumed to be an exponential function, referred to as SOL11 in Fig. 11(b). Although the scalelength of the exponential function was selected to match the profile measured at the outboard mid-plane, it did not incorporate the actual SOL plasma geometry, such as the divertor X-point. In order to investigate the importance of SOL geometry, a new SOL model was incorporated into GENRAY/CQL3D [42]. The model uses a measurement of T_e and n_e on the midplane and T_e on the divertor tiles (the so-called “two point model”), and computes the density and temperature elsewhere along the field line based on pressure conservation along the field line and classical Spitzer parallel heat conduction. As shown in Fig. 11(a), the new SOL profile is significantly different near the divertor region. This improved model for the SOL predicts a more significant reduction of current drive as the

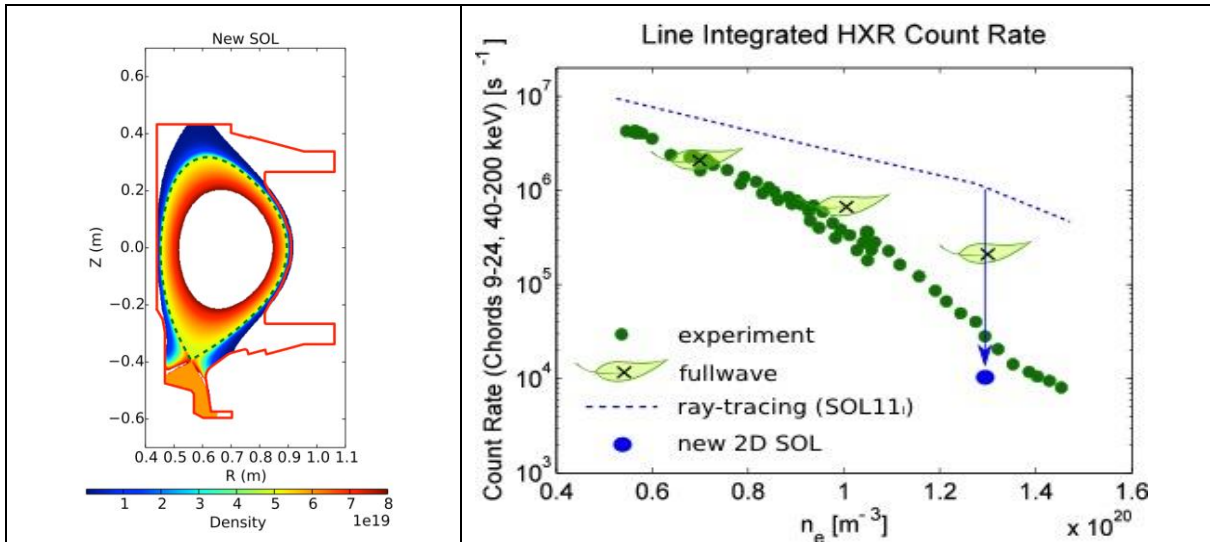


Figure 11. (a) New SOL model employed in GENRAY. (b) GENRAY/CQL3D prediction of HXR emission intensity when 2D realistic SOL is used (blue). Also shown are the experimental HXR count rates in green, the simulated HXR count rates using the simplified SOL model (SOL11) in GENRAY, and the HXR counts predicted by the LHEAF full-wave LH solver which includes a simplified SOL.

density is increased compared to previous work [43] and is more consistent with experiment [42] (see Fig. 11(b)).

3.3 Ray tracing / Fokker Planck analysis of JET discharges at high density

In JET, a new Ray Tracing (RT)/ Fokker-Planck (FP) package (JRT), with a real 2D geometry accounting for the plasma boundary and launcher shape and a new 3D relativistic bounce averaged FP code, has been developed [44] for LH power deposition analysis and the main results are shown in Fig. 12. Power deposition profiles from the code are compared to experimentally assessed profiles from modulated LH experiments [45] and ECE analysis data [46]. Calculations are in a reasonable agreement with experimental data at low density (discharge #77609, $n_e \approx 2.4 \times 10^{19} \text{ m}^{-3}$) and high density (discharge #77612, $n_e \approx 3 \times 10^{19} \text{ m}^{-3}$). The code cannot reproduce absorption at the cold periphery ($0.6 < \rho < 0.8$) in both cases whereas in addition to this at high density (#77612) the calculated core absorption ($\rho < 0.2$) is much higher than experimental results. Simulations with broadened initial $N_{||}$ spectra (i.e. upshift of $N_{||}$ up to 2.5) resulted in more consistent deposition in the periphery with numerical results matching experimental data up to $\rho \approx 0.7$.

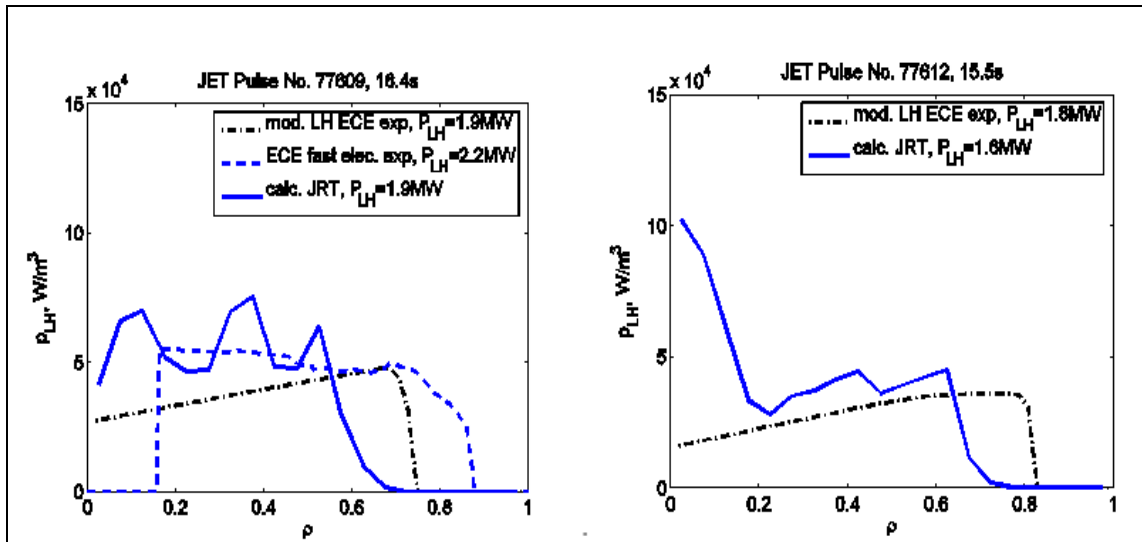


Figure 12. LH wave power deposition profiles of JET for 3.4T/1.5MA, line averaged $n_e = 2.4 \times 10^{19} \text{ m}^{-3}$, central $T_{e0} = 3 \text{ keV}$, low density pulse #77609 (left figure) and for 3.4T/1.8MA, line averaged $n_e = 3.0 \times 10^{19} \text{ m}^{-3}$, central $T_{e0} = 3.5 \text{ keV}$, high density pulse #77612 (right figure). The power deposition profiles, provided by JRT code, p_{LH} (solid blue lines), were calculated with real $N_{||}$ spectra of the launched waves. The experimental profiles provided for comparison were determined from LH modulation experiments (dash-dotted black lines) [45] and alternatively from the ECE analysis of the supra-thermal electrons (dashed blue line) [46]. The total amount of experimentally assessed and calculated absorbed power, P_{LH} , is shown in the legends for all cases.

The broadening of the initial $N_{||}$ spectra in the simulations shown in Fig. 12 has been studied by examining the evolution of the rays and statistically analysing the changes in rays' $N_{||}$ during their propagation in plasma. Figure 13 shows the evolution of a typical ray, launched close to the mid-plane, $Z_0 = 0.22 \text{ m}$ with $N_{||} = 1.82$, which is representative of the maximum power spectrum. The absorption of the ray, i.e. the value of γ/ω , and its attenuation

are shown in the top two graphs for the first iteration (blue lines) between wave solver (WS) and FP code, in which case Maxwellian electron distribution function (EDF) is assumed and the final iteration (magenta lines) in which case fully evolved EDF with plateau is used in the γ/ω calculation. In the bottom graph ray's N_{\parallel} is provided together with the accessibility at the ray position, $N_{\parallel, acc}$, and the values of N_{\parallel} where good absorption is expected, which has been assessed to be at $6.5/(T_e)^{1/2}$.

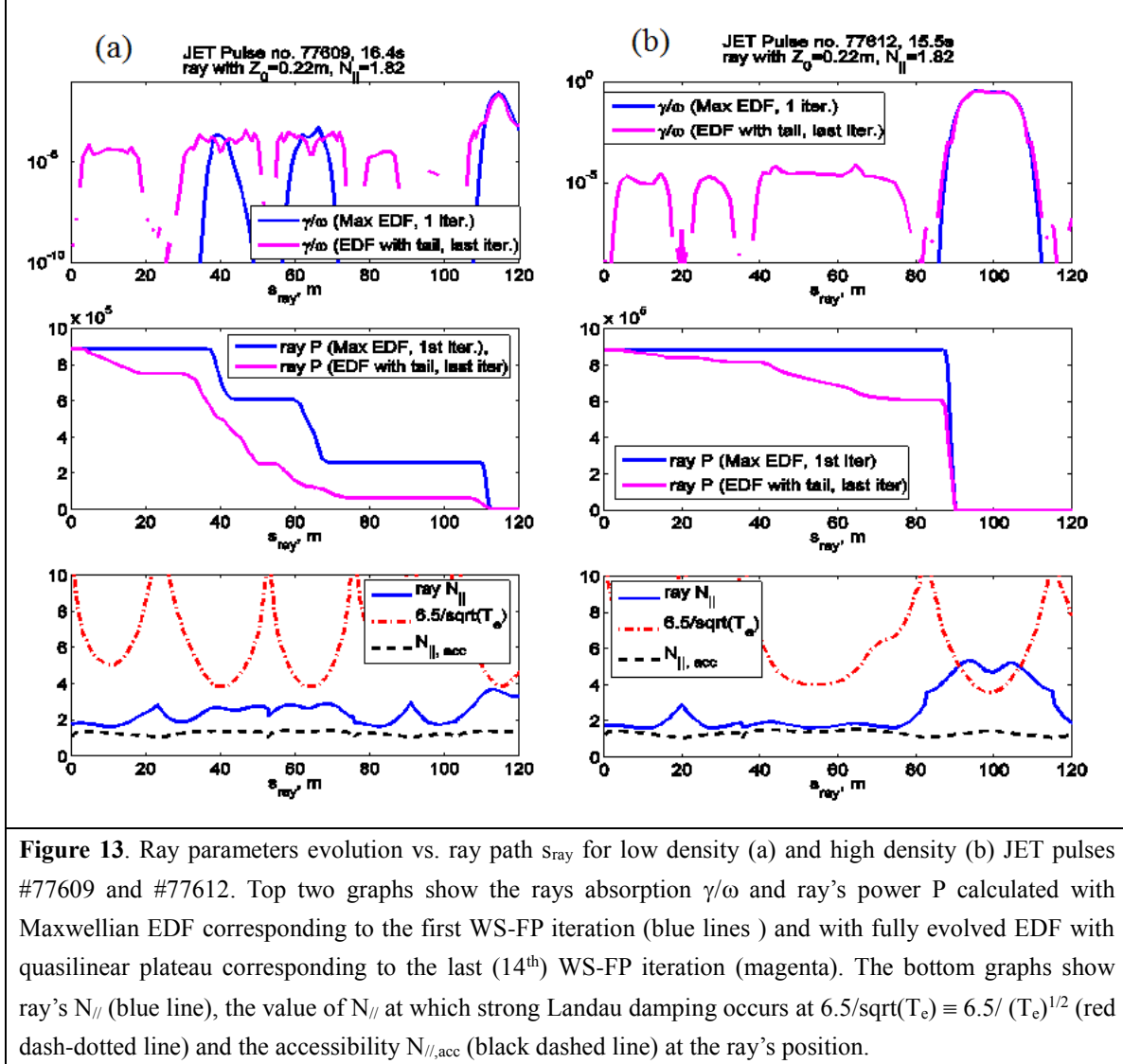


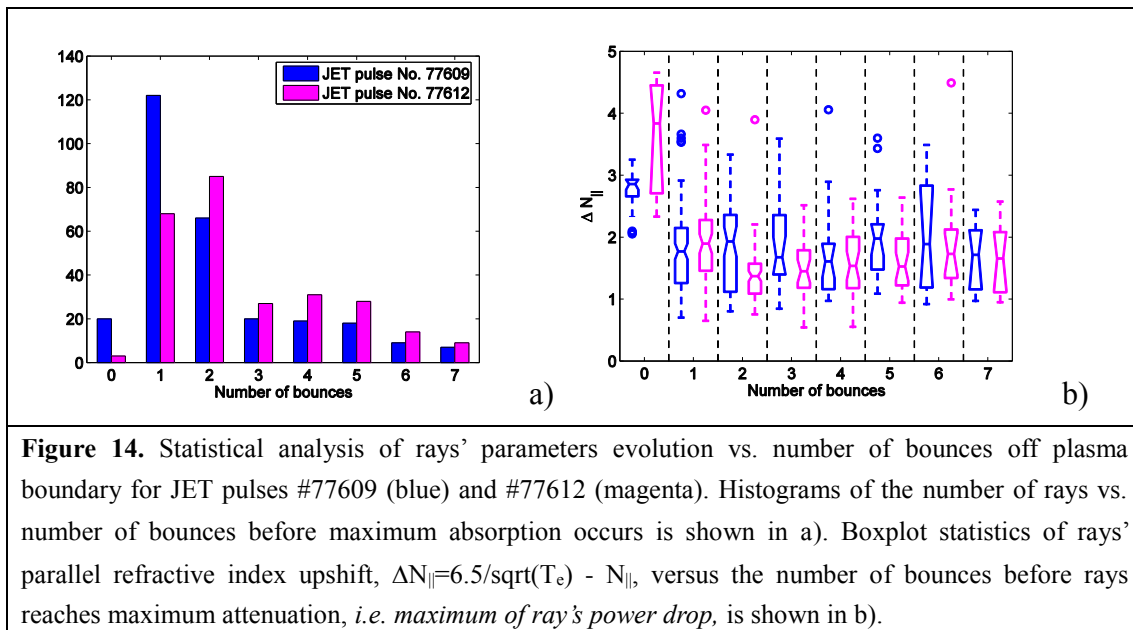
Figure 13. Ray parameters evolution vs. ray path s_{ray} for low density (a) and high density (b) JET pulses #77609 and #77612. Top two graphs show the rays absorption γ/ω and ray's power P calculated with Maxwellian EDF corresponding to the first WS-FP iteration (blue lines) and with fully evolved EDF with quasilinear plateau corresponding to the last (14th) WS-FP iteration (magenta). The bottom graphs show ray's N_{\parallel} (blue line), the value of N_{\parallel} at which strong Landau damping occurs at $6.5/\sqrt{T_e} \equiv 6.5/ (T_e)^{1/2}$ (red dash-dotted line) and the accessibility $N_{\parallel, acc}$ (black dashed line) at the ray's position.

Clearly in the low density case, JET pulse #77609 in Fig. 13(a), with wave power absorption calculated after the first WS – FP iteration (blue lines), an upshift in N_{\parallel} is required for the ray power to be fully absorbed, which happens for $N_{\parallel} \sim 2.7$ ($s_{ray} \sim 40m$ and $s_{ray} \sim 65m$) near the local minima of the quantity $6.5/(T_e)^{1/2}$, estimated to be about 3.8. After the last WS – FP iteration EDF is fully evolved, with a quasilinear plateau. This allows ray's power absorption to happen for lower N_{\parallel} as seen from the magenta lines in Fig. 13(a). The bottom graph shows that with fully evolved EDF ray absorption occurs in a wider range around local $6.5/(T_e)^{1/2}$ minima, implying larger difference between $6.5/ (T_e)^{1/2}$ and N_{\parallel} in the absorption zone. In this example the ray stays well above its local accessibility refractive index, $N_{\parallel, acc}$, as

shown in the bottom graph and never mode-converts to fast wave. Nearly all of the LH slow wave power, $\sim 86\%$, is absorbed before first mode conversion of the rays.

It is important to note the central electron temperature was comparable in these two cases despite the difference in density. In the low density discharge the central electron temperature was of the order of $T_{e0} \approx 3$ keV, i.e. a relatively cold plasma in L-mode with a small amount (<1.4 MW) of NBI power for diagnostic purposes. In the higher density case with H-mode like density pedestal a higher central electron temperature $T_{e0} \approx 3.5$ keV was achieved by applying ~ 9.5 MW of NBI power.

In the high density case, JET pulse #77612, Fig. 13(b), the ray requires significant N_{\parallel} upshift for the ray's power to be fully absorbed. This happens at $s_{\text{ray}} \sim 90\text{m}$ for $N_{\parallel} \sim 4.6$, which value is again close to the local minimum of $6.5 / (T_e)^{1/2} \sim 5.5$. Using the fully evolved EDF as provided after the last WS – FP iteration allows some ray power absorption to happen for lower N_{\parallel} (see Fig. 13(b) magenta) but a considerable amount of power remains until N_{\parallel} upshifts again to about 4.6 where it is eventually absorbed. The difference in N_{\parallel} at which LH wave power is absorbed in the two cases, ~ 2.7 for #77609 and ~ 4.6 in #77612, is considerable in terms of velocity of the resonant electrons, which scales as c/N_{\parallel} . For most of its propagation the ray stays close to $N_{\parallel, \text{acc}}$, but it mode-converts to fast wave at the very end, $s_{\text{ray}} > 120\text{m}$ (not shown in the graph), after all power is fully absorbed. About half of the LH slow wave power, $\sim 48\%$, is absorbed before first mode conversion of the rays.



Statistical analysis, Fig. 14, of all 288 rays used in both calculations supports the conclusions stated above. Results shown in Fig. 14 are for the case with fully evolved EDF as provided by the last WS – FP iteration. As shown in Fig. 14(a), histograms most of the rays need 1-2 bounces before experiencing maximum absorption. For pulse #77609 significantly more rays are absorbed after just one bounce, Fig. 14(a), while at high density pulse #77612 the number of rays requiring 2 to 5 bounces to reach maximum absorption is much higher meaning higher probability of N_{\parallel} upshift. In Fig. 14(b) the number of rays' bounces before maximum absorption of the rays occur is analysed versus rays' N_{\parallel} evolution. As a measure of

the latter we use the difference $\Delta N_{\parallel} = 6.5 / (T_e)^{1/2} - N_{\parallel}$ at the location of the maximum rays' absorption. In the lower density case #77609 [blue lines in Fig. 14(b)] the ΔN_{\parallel} averaged over all rays is about 1.9 while for #77612 [magenta lines in Fig. 14(b)] this number drops to 1.6. For rays requiring two or more bounces the difference ΔN_{\parallel} is lower for high density cases meaning that higher N_{\parallel} upshift in this case. Interestingly, for rays requiring just one bounce off the plasma boundary before reaching maximum absorption the averaged ΔN_{\parallel} values are approximately the same, ~ 1.8 , in both cases.

To summarise, one can conclude that indeed the initial N_{\parallel} spectrum upshifts during rays' propagation and this is better pronounced at higher densities, where in general rays bounce more before being absorbed. In addition, at higher density the effect of N_{\parallel} upshift is better pronounced as rays' power is absorbed for lower ΔN_{\parallel} , i.e. closer to the local value of $6.5/(T_e)^{1/2}$ compared to the low density case.

3.4(a) Analysis of PI in two-frequency LHCD discharge in EAST

Previous experiments on FTU indicated that SDF would not play a significant role in tokamak experiments performed so far at high plasma densities, since LHCD effects (as inferred from hard x-ray emission) occurred at very high density ($n_e = 2 \times 10^{20} \text{m}^{-3}$, with ITER-relevant n_e profile and high T_e periphery regime) in the presence of a RF probe spectrum that was symmetrically broadened (up to 7 MHz), attributable to SDF [8]. Conversely, a significantly broadened and downshifted spectrum (up to 15 MHz), not accompanied by any LHCD effect in plasma was produced in standard high-density regime, consistent with PI modelling results [8]. Based partly on the FTU results we are thus motivated to analyze the possible role of PI in the EAST two-frequency discharge.

Modeling of PI using the LHPI code [30] and a growth-rate solver [31][32] originally based on the parametric dispersion relation derived by Porkolab [33], that has been extended [32] to include another form of the dispersion following the approach in Liu [34], are qualitatively consistent with the measured RF spectrum. Using this solver, recent investigations have focused on the parametric excitation of the LH wave (sideband) in the parallel coupling limit. In this limit, the excited sideband LH wave can propagate nearly along the launched LH pump wave. Since the sideband can be excited and its amplitude can grow only in the presence of the pump, this parallel coupling case could result in a higher sideband amplitude in high density plasmas for which the pump wave has a limited radial penetration and spends longer time at the plasma edge where it is unstable to parametric instabilities. Figure 15 shows an example of the normalized frequency (ω_R / ω_{ci})

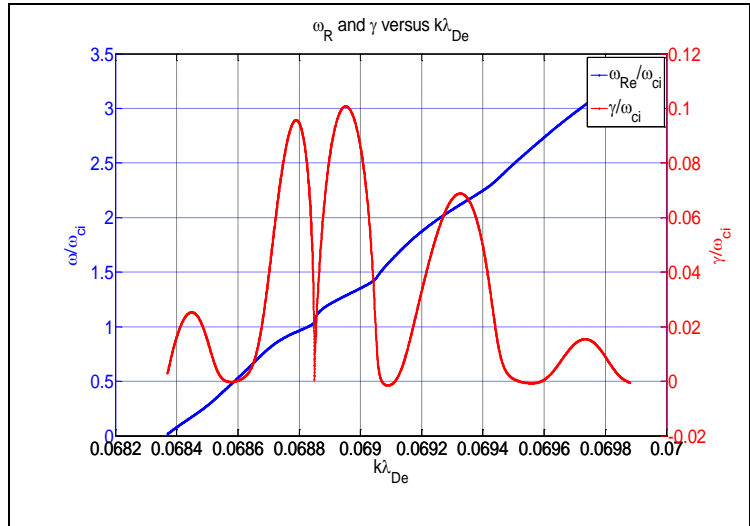
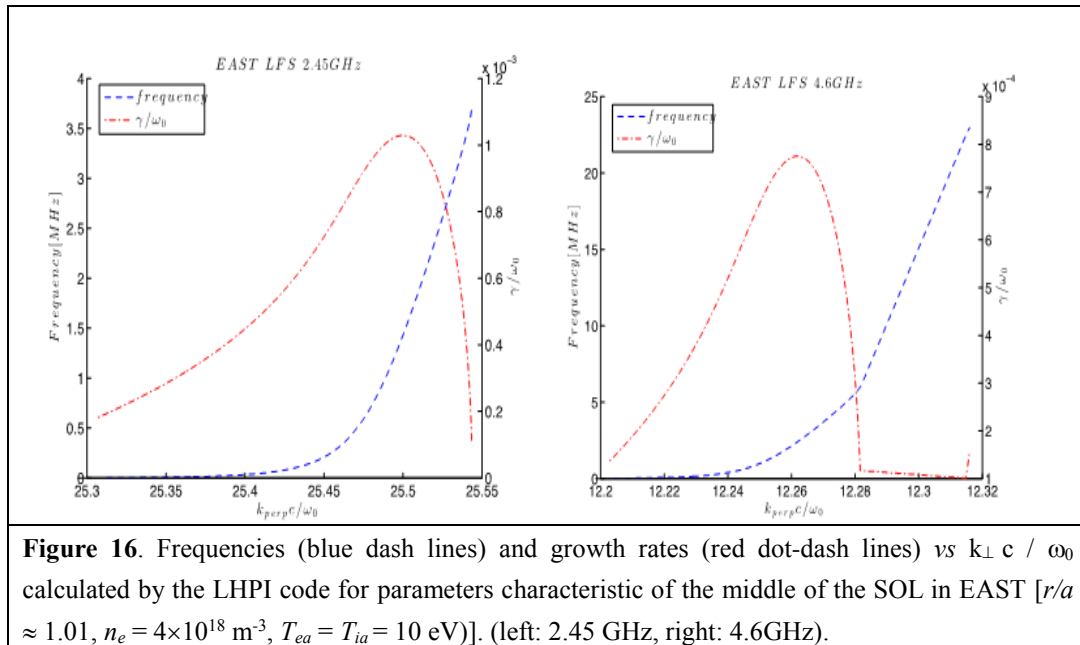


Figure 15. Growth rate calculation for pump frequency $f_0 = 2.45$ GHz, $n_e = 3 \times 10^{18} \text{m}^{-3}$, $T_e = T_i = 50$ eV, $B = 2.8$ T, $ck_{\parallel 0}/\omega_0 = 2.1$ (pump wave), $ck_{\parallel}/\omega_0 = 7$ (sideband), $P = 3.2$ MW/m².

and growth rate (γ / ω_{ci}) spectra when $\theta = 10$ deg. in EAST. In this particular case, one interesting feature is the appearance of a dip in the growth rate spectrum around the ion cyclotron first-harmonic solution ($k\lambda_{DE} \approx 0.06883$). This dip is due to the upper sideband also being nearly resonant ($|\varepsilon^+| \approx 0$), which is generally off-resonant and does not contribute much in determining γ in the limit $\theta \rightarrow 90$ deg.

Based on the experiments in Sec. 2.1, the effect of LH frequency (2.45 GHz and 4.60 GHz) on PI in EAST has been analysed. Considering the typical EAST plasma with a line-averaged plasma density of $2 \times 10^{19} \text{ m}^{-3}$ and using the LHPI code, the calculated frequencies and growth rates of PI driven mode are shown in Fig. 16, in which the RF coupled power of 1MW, the antenna power spectrum peak ($N_{//0} = 2.0$) and the EAST antenna dimensions have been considered. For the pump frequency of 4.60 GHz, the analysis performed by the LHPI code shows that the PI mechanism is mostly driven by a low frequency quasi-mode in the range of ion-sound evanescent modes (of about 2 MHz), consistent with the observed phenomenon of spectral broadening. Assuming kinetic radial profiles merging the available data of the SOL and main plasma, for the case of 2.45 GHz, the normalised maximum homogeneous growth rate in the middle of the SOL (at $r/a \approx 1.01$, $n_e = 4 \times 10^{18} \text{ m}^{-3}$, $T_{ea} = T_{ia} = 10 \text{ eV}$) reduces from $\gamma / \omega_0 \approx 1 \times 10^{-3}$ (see Fig. 16) by about a factor two at $r/a \approx 0.8$, and is still positive at $r/a \approx 0.5$. In contrast, for 4.60 GHz, the corresponding value in the middle SOL is smaller (by about 20%, see Fig. 16), reduces by about a factor of three at $r/a \approx 0.8$, and the plasma becomes stable (i.e., the growth rate is negative) for $r/a < 0.7$. Since PI occurrence is regulated by convective losses [34][30], these results suggest that the phenomenon should be less pronounced for the case of 4.60 GHz, because the wave group velocity is higher at higher frequency, resulting in the wave staying in the convective growth region for less time.



Calculations with the parametric dispersion code described in [31][32] at frequencies of the PI driving mode near the first ion cyclotron harmonic show that the growth rate is positive and finite for both 2.45 GHz and 4.6 GHz but reduces by a half at 4.6 GHz (see Fig. 17). Additionally a scan was done of power density for each of the LH grill launchers which

suggests that PI instability will occur even down to the lowest power density examined as can be seen in Fig. 17. For each frequency case examined the actual grill area was used corresponding to 0.202 m² for the 2.45 GHz launcher and 0.198 m² for the 4.6 GHz launcher while injected LH powers of (0.2, 0.4, 1.0) MW were used with each frequency. For each of the parametric dispersion calculations shown in Fig. 17 the electric field is found from the WKB approach and the perpendicular wavenumber of the lower sideband is assumed to be normal to the perpendicular wavenumber of the pump wave. Results for the computed growth rate at 0.4 MW are not shown in Fig. 17, although those growth rate values were found to lie between the 1.0 MW and 0.2 MW cases.

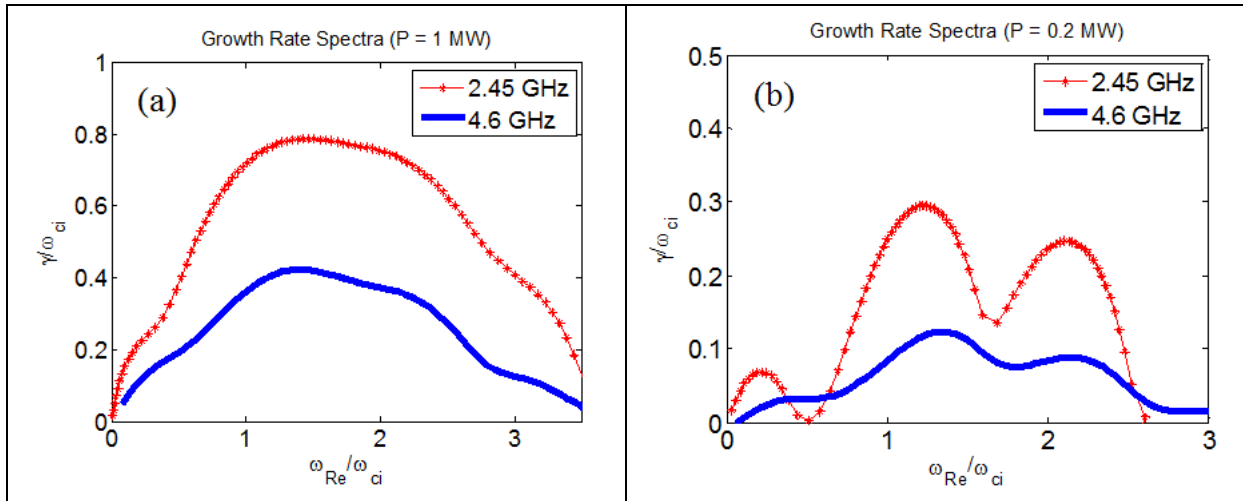


Figure 17: Computed growth rate spectra with $f_0 = 2.45$ GHz (red asterisk) and 4.6 GHz (blue line) using the parametric dispersion code described in [31][32]. The parameters assumed are deuterium plasma, $n_e = 5 \times 10^{18}$ m⁻³, $T_e = T_i = 30$ eV, $B_t = 1.83$ T, $N_{//0} = 2$, and the ion mode $N_{//} = 7$. (a) 1 MW injected LH power with $P_{RF, 2.45 \text{ GHz}} = 4.95$ MW/m² ($= 1$ MW / 0.202 m²) and $P_{RF, 4.6 \text{ GHz}} = 5.05$ MW/m² ($= 1$ MW / 0.198 m²). (b) 0.2 MW injected LH power with $P_{RF, 2.45 \text{ GHz}} = 0.99$ MW/m² ($= 0.2$ MW / 0.202 m²) and $P_{RF, 4.6 \text{ GHz}} = 1.01$ MW/m² ($= 0.2$ MW / 0.198 m²).

3.4 (b) Power spectrum analysis of two-frequency LHCD discharge in EAST

The two-frequency LHCD experiment performed in EAST is based on the use of two different antennas, whose geometrical characteristics may have a direct impact on the coupled power spectra and the overall ray-tracing/Fokker-Planck simulations. It is therefore critically important to evaluate them carefully with a rigorous procedure, taking into account of the operating conditions at the times considered for the simulations. This is carried out with ALOHA coupling code running in 1-D mode [16], using experimental input powers and phases of each module and for each row. The latter are accurately measured just in front the ceramic window. The density in front of each row is determined by minimizing the difference between calculated and measured reflected power levels in each module, keeping the density scale length to its default value $\lambda = n/\nabla n = 0.02$ m, as calculations are rather weakly sensitive to this parameter. From EAST LH experiments, the low density solution of the reflection coefficient (RC) is considered, since moving away antennas from the plasma separatrix leads systematically to a degradation of the coupling conditions. Once the density is

self-consistently determined, the power spectrum is evaluated for each row, and the global power spectrum for the whole antenna is evaluated by summing over all antenna rows of waveguides. This procedure is preferred to the one considering direct measurements of the density by Langmuir probes. Indeed, the density may change significantly along the poloidal direction, and measurements are too sparse for an accurate determination of the power spectra, as required by calculations of the RCs. Nevertheless, the densities self-consistently determined from RCs for the 2.45 and 4.6 GHz antennas, $1.0 \times 10^{17} \text{ m}^{-3}$ and $5.0 \times 10^{17} \text{ m}^{-3}$ respectively, are found to be reasonably close to Langmuir measurements of the order of $1.0 \times 10^{18} \text{ m}^{-3}$, as shown for Tore Supra LH studies [47]. The input power spectra by ALOHA for antennas at 2.45 GHz and 4.6 GHz are shown in Figs. 18(a) and 18(b). Here, the spectrum is expressed as a function of the refractive index component along the toroidal direction (Fourier transform along this direction), n_z , since a simplified slab geometry is assumed at the plasma edge near the grill without any poloidal dependence. As far as the safety factor is high enough near the separatrix, $N_{//}$ may be reasonably approximated to n_z , since the poloidal field component is very small as compared to the toroidal one. However, when B_z/B_p is becoming significant, a correction must be considered, and $N_{//} = n_z * B_z/B_p$, where B_z and B_p are the toroidal and poloidal components of the magnetic field amplitude (B), respectively.

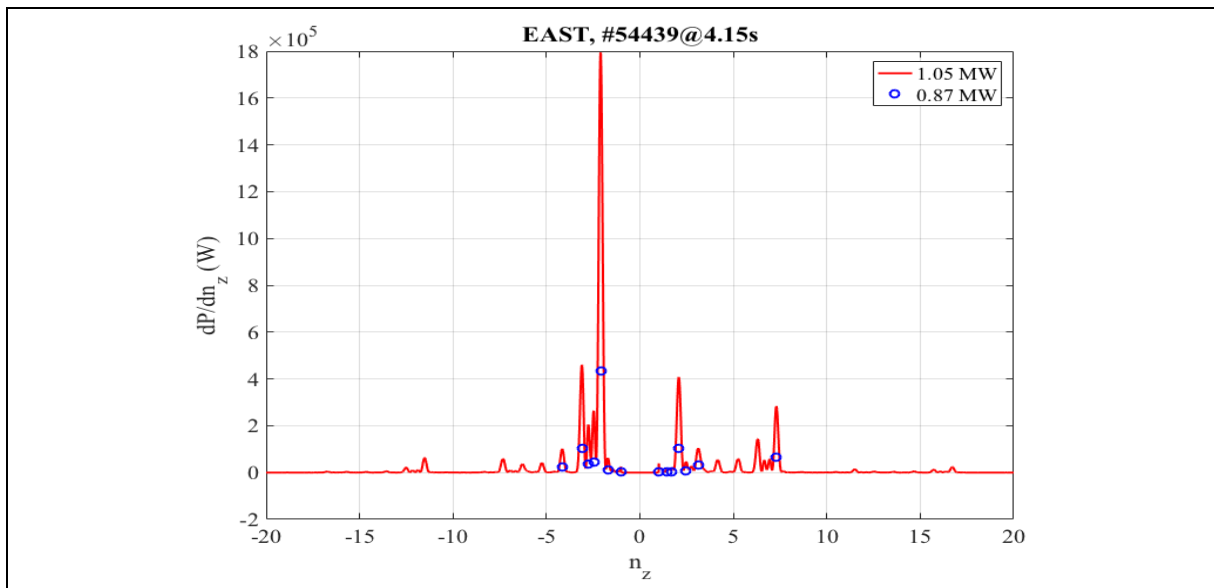


Figure 18(a). Power spectrum for the 2.45 GHz antenna evaluated by ALOHA 1-D code. The density in front of the antenna is about $1.7 \times 10^{17} \text{ m}^{-3}$. Blue circles correspond to the prominent lobes for current drive considered for ray-tracing calculations. With 14 selected lobes, the effective power available for current drive calculation is 0.87 MW, while power carried by all lobes is 1.05 MW. The lobe selection preserves antenna directivity.

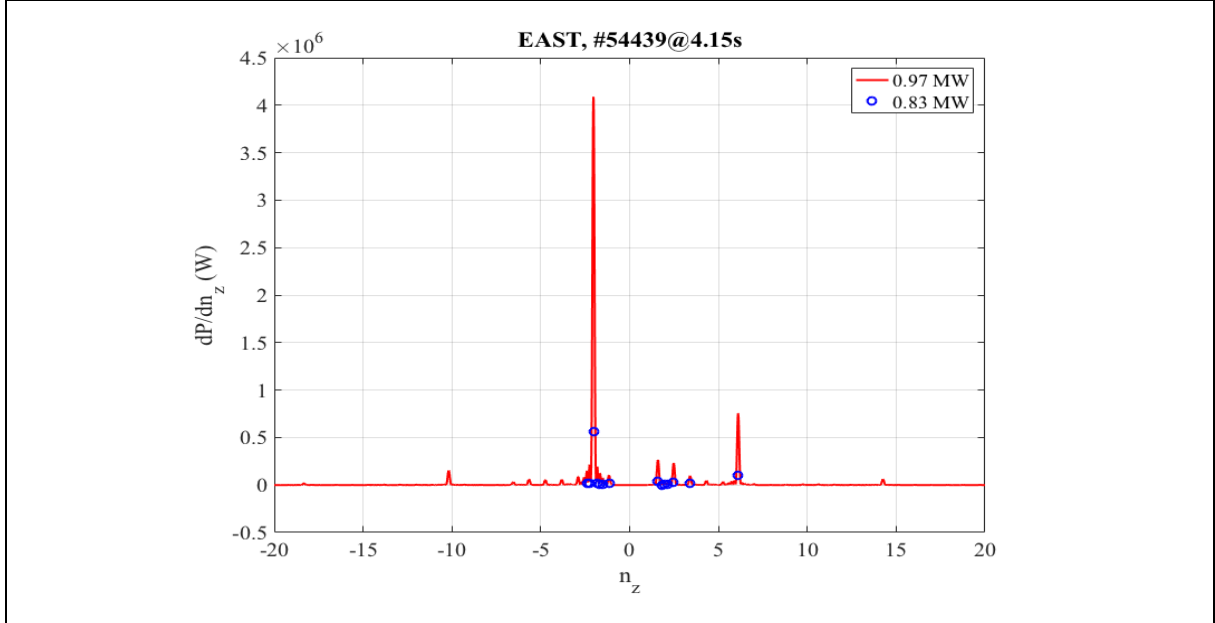


Figure 18(b). Power spectrum for the 4.6 GHz antenna evaluated by ALOHA 1-D code. The density in front of the antenna is about $5 \times 10^{17} \text{ m}^{-3}$. Blue circles correspond to the prominent lobes for current drive considered for ray-tracing calculations. With 14 selected lobes, the effective power available for current drive calculation is 0.83 MW, while power carried by all lobes is 0.97 MW. The lobe selection preserves antenna directivity.

Due to the rather large RCs for the 2.45 GHz antenna, reaching 10% approximately, multiple satellite lobes appear, either at high- N_{\parallel} in the co-current side ($N_{\parallel} < 0$) and counter-current side ($N_{\parallel} > 0$), leading to an overall degradation of the power in the main co-current lobe of the 2.45 GHz antenna, as compared to the antenna at 4.6 GHz where the power in the main co-current lobe is higher at same input power level.

3.4(c) Ray tracing / Fokker analysis of two-frequency LHCD discharge in EAST

From standard ray-tracing/Fokker-Planck calculations using C3PO/LUKE codes based on the power spectra determined as explained in the previous section, the LH-driven currents are estimated to be 85 kA at 4.15s for the 2.45 GHz antenna and 94 kA at 5.15s for the 4.6 GHz antenna [48]. Such a result is consistent with the larger loop voltage drop at 5.15s, which indicates better current drive efficiency when operating with the 4.6 GHz antenna. This result is obtained despite the larger measured effective charge, Z_{eff} , when using the 4.6 GHz antenna, which increases from 2.8 to 3.0 at the considered time slices. The non-resonant collisional absorption at the plasma edge is found negligible, therefore $\sim 100\%$ of the LH power coupled to the plasma is absorbed by Landau resonant absorption in the calculations. As noted above, these simulations did not employ a “tail” in the LH power spectra. Also fast electron transport was turned off in the Fokker Planck code (LUKE).

Ray tracing/Fokker Planck calculations using the GENRAY/CQL3D codes have also been carried out for the same plasma profiles, MHD equilibrium, and LH power spectra that were used in the C3PO/LUKE simulations of LH current drive for the 2.45 GHz antenna at 4.15s and the 4.6 GHz antenna at 5.15s described above. The total driven LH current in the absence of the DC electric field was found to be about 130 kA in the case of each frequency with the

4.6 GHz current profile peaked farther off-axis than the 2.45 GHz as can be seen in Figs 19(a) and 19(b).

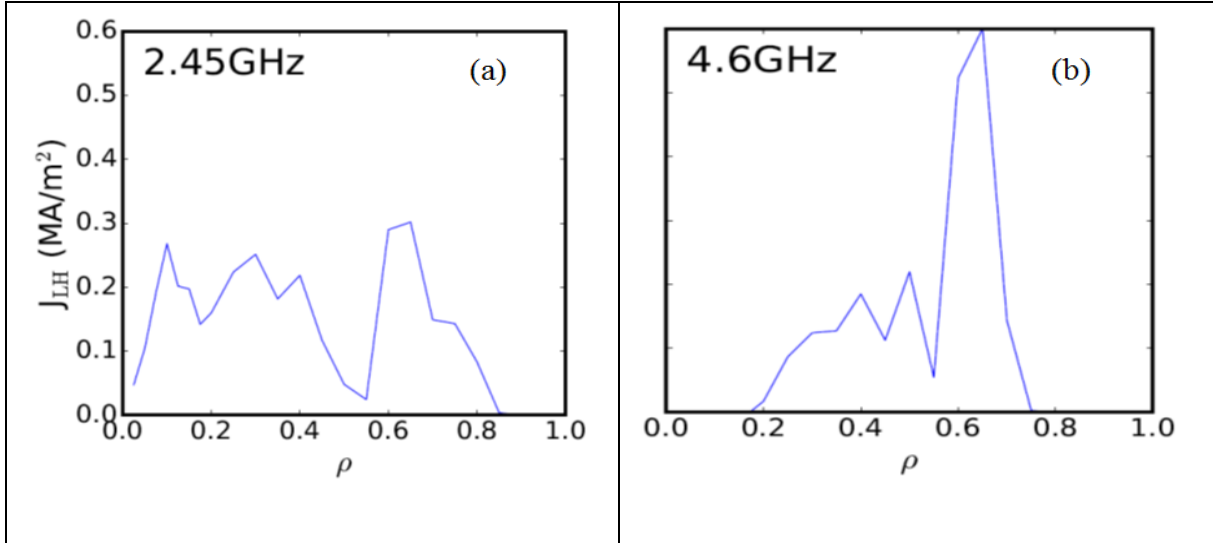


Figure 19. GENRAY / CQL3D simulations of LH current drive in EAST using LH power spectra from the ALOHA code shown in Fig. 16 with zero DC electric field for the (a) 2.45 GHz antenna at 4.15s and for the (b) 4.6 GHz antenna at 5.15s. The total LH current in each case is ~ 130 kA.

Note that without loop voltages, but considering the same magnetic MHD equilibrium and initial ray conditions, GENRAY/CQL3D and C3PO/LUKE calculate different current density profiles for the two cases here considered, though some similarities are observed when the LH frequency is increased from 2.45 to 4.6 GHz. Indeed, power absorption is more central and broad for 2.45 GHz, while it is more off-axis at 4.6 GHz for both codes. The differences between predictions may result from several reasons, like the different number of rays used in the simulations, the spectral width for each ray, which may impact quasi-linear convergence. Despite accurate benchmarks and the excellent agreement between the two set of codes in the linear limit like for the LH wave in ITER[1], the very sensitive weak absorption regime here considered, may reveal some differences in their use. This is likely an indication of the limit of prediction of these numerical tools when conditions of applicability become marginal.

3.4 (d) Current prediction in presence of a residual Ohmic electric field

With a residual Ohmic electric field corresponding to $V_{loop} = 0.27$ V and $V_{loop} = 0.15$ V at 4.15s and 5.15s respectively, while LH power is applied, synergistic effects must be considered to evaluate the total driven current.

In a preliminary study, the time evolution of the #54439 discharge is calculated with the METIS code [49], thus allowing to determine the global consistency between different measurements, using simple 1-D fluid model. In this simulation, the loop voltage is determined to match the observed current level, while temperature is determined from transport calculations using prescribed density and Z_{eff} profiles.

As shown in Fig. 20, in the Ohmic phase after the current flat-top, the predicted loop voltage is more than twice the observed V_{loop} level, as well as the total energy content. This

discrepancy, which lasts during all the discharge, including during application of the LH power using a coarse scaling law for the current drive efficiency determined from LH experiments in Tore Supra tokamak [50], may be ascribed (for example) to the existence of a population of runaway electrons generated in the start-up phase of the discharge. Consistently, using LUKE or CQL3D Fokker-Planck codes, the predicted current in the Ohmic phase is far too low (< 200 kA) as compared to observation using the experimentally measured $V_{\text{loop}} = 0.8$ V and $Z_{\text{eff}} \approx 2.0$, while the predicted current level is rather close to experimental value $I_p = 430$ kA, when V_{loop} is twice larger, close to the value determined by METIS code. If one considers error bars on the electron temperature and Z_{eff} measurements it is possible to increase the peak electron temperature from 0.9-1.0 keV to ~ 1.2 keV and reduce Z_{eff} from 2.0 to ~ 1.8 , in which case the predicted ohmic current from LUKE and CQL3D increases to ~ 370 kA, which is much closer to the experimental value of 430 kA.

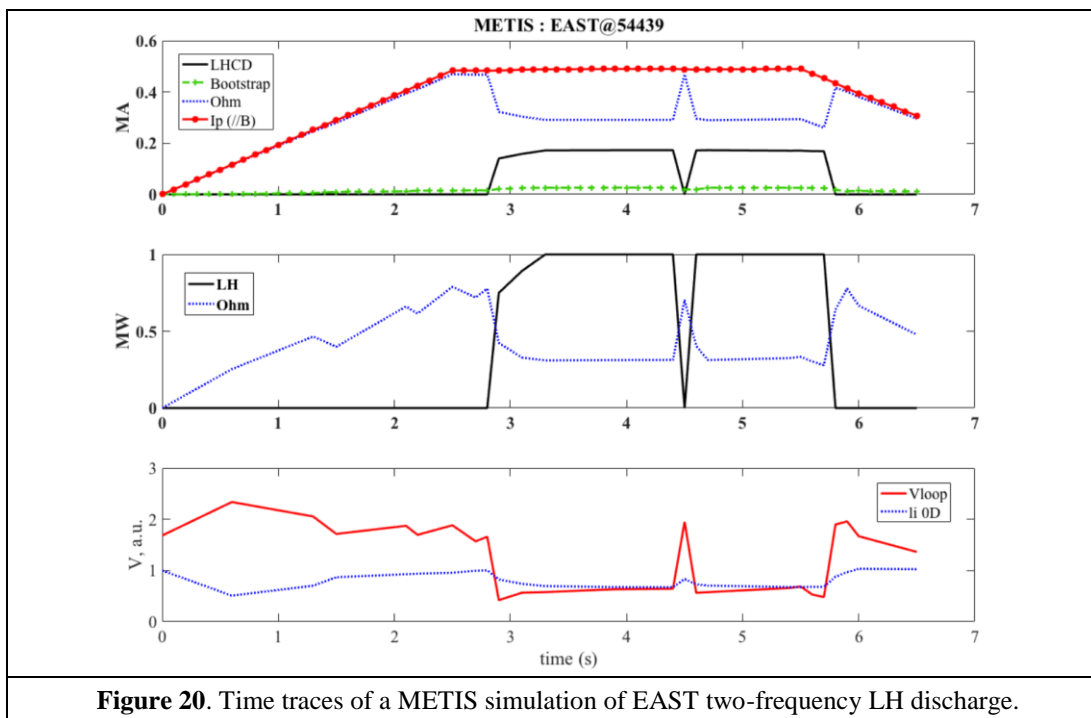


Figure 20. Time traces of a METIS simulation of EAST two-frequency LH discharge.

From C3PO/LUKE calculations, the loop voltage at 4.15s and 5.15s are evaluated to match the experimental plasma current $I_p = 430$ kA and Z_{eff} ($= 2.8$ at 4.15s and $= 3.0$ at 5.15s), taking into account of synergistic effects. The electric field profile is taken flat over the plasma. With the 2.45 GHz antenna, $V_{\text{loop}} = 0.7$ V (close to METIS code value), while $V_{\text{loop}} = 0.58$ V for the 4.6 GHz antenna. The drop of loop voltage of the order of 0.12 V is consistent with observation and the total plasma current is well retrieved.

Power absorption and current density profiles at 4.15s and 5.15s are displayed in Figs. 21(a) and 21(b). Since power absorption is more off-axis with the 4.60 GHz antenna, the internal inductance is found to be lower as compared to the one corresponding to 2.45 GHz, which is not consistent with observations. However, the detailed characteristic of the current density profiles in the outermost part of the plasma is usually difficult to model, leading to a large uncertainty on the predicted internal inductance level. Nevertheless, the order of magnitude of the measured value is rather well recovered by calculations, especially considering how

sensitive the internal inductance is to variations in the current density profile at large radii ($0.6 < r/a < 1.0$).

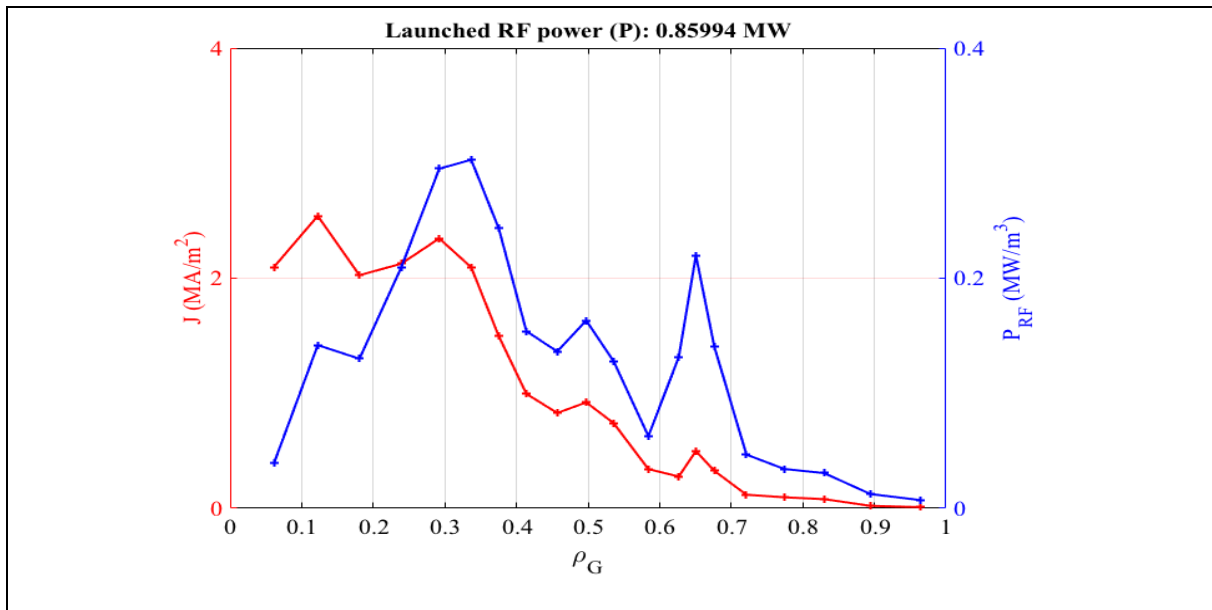


Figure 21(a). Power absorption and current density profiles for the 2.45 GHz antenna evaluated by C3PO/LUKE codes. The calculated internal inductance is about 1.53, while experimental value is 1.25 approximately.

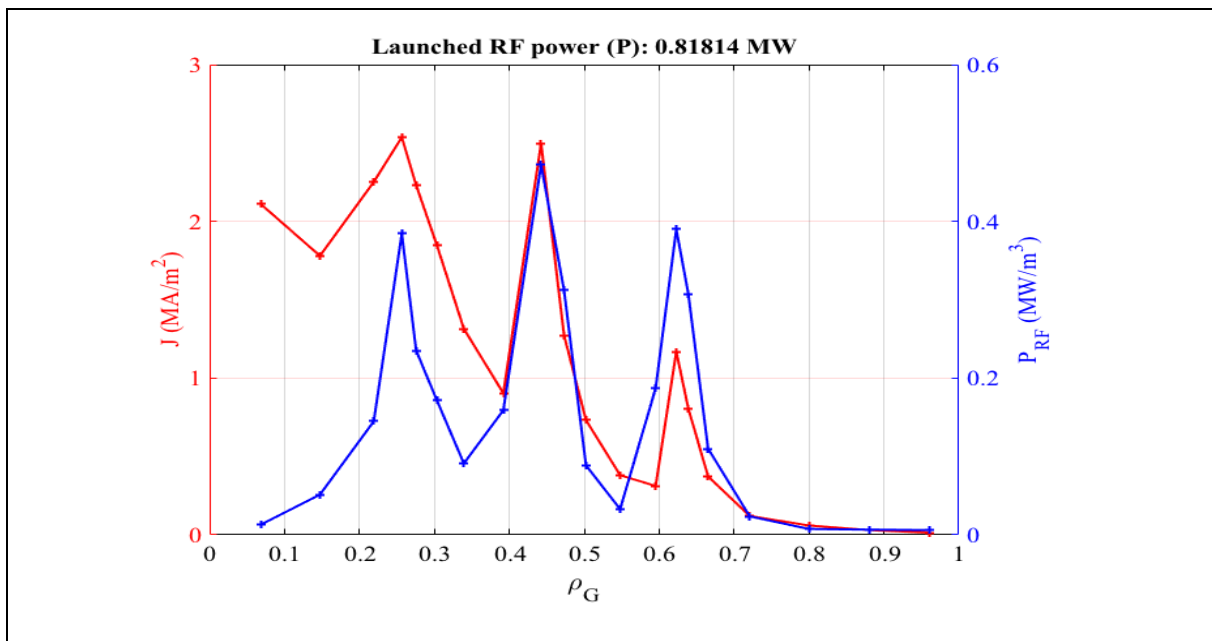


Figure 21(b). Power absorption and current density profiles for the 4.6 GHz antenna evaluated by C3PO/LUKE codes. The calculated internal inductance is about 1.31, while experimental value is 1.3 approximately.

Uncertainties in the measurement of Z_{eff} have already been discussed earlier in terms of how they can impact the predictions of plasma current during the Ohmic phase. Such uncertainties can also affect discharge simulations during the phase with LHCD injection. For example Fig. 22 shows the predictions of LHCD from GENRAY/CQL3D with 2.45 GHz power (4.15s) and 4.6 GHz power (5.15s), where now $Z_{\text{eff}} = 2.1$ (near its Ohmic value) has been assumed and the actual experimental values of loop voltage were used at 4.15s ($V_{\text{loop}} = 0.27$ V) and at 5.15s ($V_{\text{loop}} = 0.15$ V). In this case the integrated LH currents at 2.45 GHz and 4.6 GHz were found to be 460 kA and 416 kA respectively, thus the ray tracing / Fokker Planck model was found to approximately give the experimental current of 430 kA sustained with both LH systems using the experimental loop voltages and a lower Z_{eff} . If the same Z_{eff} is used as that in Fig. 21, we find the total (LH plus Ohmic) current drops by about 20%. Although the total current predicted by LUKE/C3PO and GENRAY / CQL3D are different in magnitude, the conclusion is the same from both models, namely the total current from ohmic and LH is comparable for both the 2.45 GHz and 4.6 GHz systems.

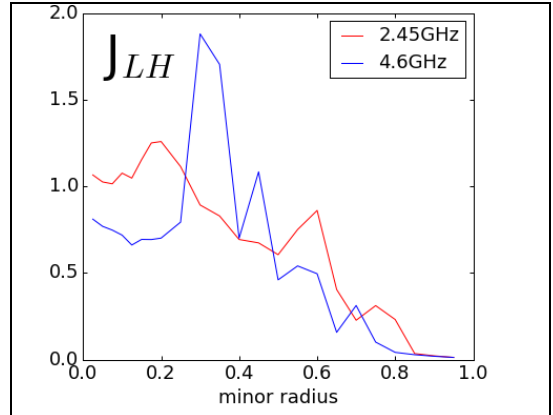


Figure 22. GENRAY/CQL3D simulation of EST two-frequency LHCD discharge #54439. LH current density profiles versus normalized radius. Red curve corresponds to 2.45 GHz injection at 4.15 s and blue curve corresponds to 4.6 GHz injection at 5.15s.

The study of the two-frequency EAST LH discharge has highlighted the need to perform time dependent simulations prior to detailed time slice studies, in order to cross-check the veracity of the discharge, i.e. the consistency between quantities that play a critical role in current drive calculations. In particular, the ability to reproduce an Ohmic phase is essential to validate further LH discharges with non-negligible residual loop voltage. The procedure here considered, using ALOHA code for power spectra, METIS code for global discharge simulation, and ultimately C3PO/LUKE and GENRAY/CQL3D for current drive calculations, demonstrates the importance of verifying the self-consistency of input data that one employs in such analyses. In addition, the variation of measured quantities within error bars was also found to be important, *e.g.* the variation of Z_{eff} .

4. Conclusions and discussion

Experimental and simulation / modeling results have been presented for lower hybrid current drive in discharges on the Alcator C-Mod, EAST, and JET, tokamaks. Taken together these results represent significant progress in understanding LHCD at densities where off-axis current profile control would be needed in the ITER device and beyond. Although these experiments were carried out over a wide range of density (factor of ten) and toroidal magnetic field (factor of five) they can all be meaningfully compared with each other in terms of the dimensionless parameter ($f_{\text{pe}} / f_{\text{ce}}$) which determines wave accessibility and wave refraction (see Fig. 1). The primary challenge in understanding these experiments is they all occur in electron temperature regimes where the LH wave is not fully absorbed in a

single pass into the plasma core and thus the role of the scrape off layer (SOL) in determining wave propagation and parasitic losses must be taken into account.

Experiments carried out in EAST (see Fig. 8) demonstrate the importance of SOL conditions in weak absorption regimes by comparing the efficiency of LHCD in discharges with weak and strong lithiation. Presumably in these experiments, consistent with previous results [9][8], strong lithiation reduces the wall recycling of neutrals, the edge temperature is increased and the effect of parametric instability and collisional absorption is reduced, which is beneficial for improving CD efficiency. Results from the Alcator C-Mod tokamak (see Fig. 7) demonstrate the current drive effect can be recovered at high density by increasing the plasma current from $\sim 0.6\text{-}0.8$ MA up to 1.0 MA. Higher current in C-Mod significantly decreases the scrape off layer width which places the slow wave cut-off much closer to the last closed flux surface thus minimizing the distance the LH wave may traverse in the SOL. Measurements of nonthermal ECE and hard x-ray emission in the JET device with LH power applied at high density indicate a similar loss in the CD effect as was observed in EAST and C-Mod. Analysis of the JET experiments indicates that in addition to the onset of PI, loss of wave accessibility could be an issue in these discharges. It is important to point out however that electron temperatures in a burning plasma such as ITER will be high enough to easily guarantee strong single pass damping of LH waves, thus minimizing parasitic SOL interactions, such as collisional absorption and parametric decay instabilities, unless parasitic SOL interaction occurs at the very first pass when the wave is launched .

A unique feature of the EAST facility is the capability to study LHCD using two different LH source frequencies (2.45 and 4.6 GHz) in the same discharge. Experiments carried out on EAST indicate improved CD efficiency at 4.6 GHz. Detailed modeling analysis that combines the ALOHA coupling code with the ray tracing / Fokker Planck codes LUKE/C3PO and GENRAY/CQL3D indicates this improvement can be attributed primarily to an increased power fraction in the main co-current drive lobe of the LH waveguide launcher at 4.6 GHz relative to 2.45 GHz (see Fig. 18) as well as a reduction in the growth rate of PI (see Figs. 16 and 17). The capability to apply higher frequency LH power (4.6 GHz) in EAST, thus avoiding parametric instability at higher density, has also allowed the achievement of high performance, long pulse, H-mode discharges where the plasma current is partially maintained by LHCD at $B_0=2.8\text{T}$ and line averaged densities of $\sim 4.5 \times 10^{19} \text{ m}^{-3}$ (see Fig. 5). Note that in these experiments the higher toroidal field is important for maintaining LH wave accessibility in the higher density H-mode.

The wide range of discharge conditions under which the LHCD experiments of this joint study were performed, as well as improvements in edge diagnostics, has motivated a number of innovations in the modeling and simulation tools that were applied to analyze these experiments as part of this joint study. In particular the idea of broadening the initial power spectrum up to values of N_{\parallel} near the electron Landau limit was found to yield better agreement between the measured and simulated profiles of hard x-ray emissivity in the Tore Supra, Alcator C-Mod, and EAST tokamaks (see Figs. 9 and 10). It has been proposed that this spectral broadening could occur via scattering of the LH waves from density fluctuations in the SOL or from nonlinear PI. A new model for the density and temperature profiles in the SOL based on density / temperature measurements at the divertor plates and midplane in Alcator C-Mod was implemented in a ray tracing package where it was shown that the

dramatic increase in collisional damping of rays that reached the cold dense divertor area could explain the density limit observed during LHCD in C-Mod (see Fig. 11). A new ray tracing / Fokker Planck package was also developed, which includes real 2D geometry accounting for the plasma boundary and launcher shape and a new 3D relativistic bounce averaged FP code, and was applied to JET discharges in order to understand the effect of spectral broadening on nonthermal ECE and hard x-ray emission during LHCD. A central conclusion in this study from a statistical analysis of ray behavior was that the initial power spectrum is upshifted in $N_{//}$ for both low and high density discharges that were analyzed, however the upshift is significantly more pronounced at high density where rays were found to propagate farther and undergo more reflections before being absorbed.

Finally a detailed time dependent analysis was carried using the METIS code for both the ohmic and LH driven current phases of a discharge in EAST (see Fig. 3) where two different frequency LH sources were applied. The motivation behind this analysis was primarily to determine the self-consistency between measurements of plasma current, loop voltage (and thus DC electric field), plasma charge state, plasma density, and electron and ion temperatures. It is well-known the LH current drive is a highly nonlinear function of the DC electric field, especially at lower density, and thus uncertainties in DC electric field, Z_{eff} , and electron temperature can profoundly impact the final predictions of LH current drive. It is worth noting that similar time dependent analysis was carried out using another integrated modeling suite (TRANSP + GENRAY + CQL3D) to assess how uncertainties in experimentally measured quantities affected LHCD predictions in Alcator C-Mod [51].

In conclusion, although achieving a complete understanding of the physics of LH wave propagation and absorption in present day devices is indeed a challenging problem, the prospects for application of off-axis LH current drive in a reactor grade plasma are quite promising from the standpoint of core wave physics and minimal scrape off layer interactions. The key ingredients for successful application of LHCD in a reactor will be high enough electron temperature to guarantee strong single pass damping, high enough wave frequency to avoid parametric instability, and a quiescent scrape off layer to minimize scattering from density fluctuations.

Acknowledgements:

This work is supported by the National Magnetic Confinement Fusion Science Program of China (Grant No. 2015GB102003, 2013GB106001B, 2013GB112003), the National Natural Science Foundation of China (Grant No. 11675214, 11175206, 11305211 and 11275233), the National Key R&D Program of China (Grant No. 2016YFA0400600, 2016YFA0400602 and 2016YFA0400603), Hefei Science Center CAS (2016HSC-IU008), the JSPS-NRF-NSFC A3 Foresight Program in the field of Plasma Physics (NSFC No. 11261140328), and K. C. Wong Education Foundation. Part of the work was conducted on the Alcator C-Mod tokamak, a DoE Office of Science user facility, and is supported by USDoE awards DE-FC02-99ER54512, DE-AC02-09CH11466, and DoE Grant DE-SC0010492. It is partly supported by the China-Italy and the China-France Collaboration program. We also give thanks to the support from the IOS TG of the ITPA.

This work has been carried out within the framework of the EUROfusion Consortium and has received funding from the Euratom research and training programme 2014-2018 under grant agreement No 633053. The views and opinions expressed herein do not necessarily reflect those of the European Commission. Work has been part-funded by the RCUK Energy Programme [grant number EP/P012450/1.

References:

- [1] Decker J. *et al*, 2011 *Nucl. Fusion* **51** 073025.
- [2] Cesario R. *et al*, 2013 *Plasma Phys. Contr. Fusion* **55** 045005.
- [3] Cesario R. *et al*, “Current drive for thermonuclear reactors”, to be published on *Physics Reports*.
- [4] Gormezano C. *et al*, 2007 *Nucl. Fusion* **47** S285.
- [5] Litaudon X. *et al*, 2002 *Plasma Phys. Contr. Fusion* **44** 1057.
- [6] Giruzzi R. *et al*, 2015 *Nuclear Fusion* **55** 073002.
- [7] Cardinali R. *et al*, “Radio-frequency current drive for thermonuclear fusion reactors” to be published on Scientific Reports.
- [8] Cesario R. *et al*, 2010 *Nature Communications*, 1 (5) 55.
- [9] Cesario R. *et al*, 2004 *Phys. Rev. Lett.* **92** 175002.
- [10] Bonoli P.T., and Englade, R. C. 1986 *Phys. Fluids* **29** 2937.
- [11] Peysson Y., *et al.*, 2011 *Plasma Phys. Contr. Fusion* **53** 124028
- [12] Bonoli, P.T., and Ott, E. 1982 *Phys. Fluids* **25** 359.
- [13] Fisch N. J. and Boozer A. H. 1980 *Phys. Rev. Lett.* **45** 720.
- [14] Baek S. G. *et al.*, 2016 *Phys. Plasmas* **23** 050701.
- [15] Madi M. *et al.*, 2015 *Plasma Phys. Contr. Fusion* **57** 125001.
- [16] Hillairet J. *et al.*, 2010 *Nucl. Fusion*, **50** 125010.
- [17] Liu F. K., *et al.*, 2015 *Nucl. Fusion* **55** 123022.
- [18] Li M. H. *et al.*, 2016 *Phys. Plasmas* **23** 102512.
- [19] Ding B. J. *et al.*, 2017 *Nucl. Fusion* **57** 022022.
- [20] Lyu B. *et al.*, 2014 *Rev. Sci. Instrum.* **85** 11E406.
- [21] Faust I. *et al.*, 2016 *Phys. Plasmas* **23** 056115.
- [22] Peysson Y. and the TORE SUPRA Team, 2000, *Plasma Physics and Controlled Fusion* **42** B87-B114.
- [23] Baek S.G. *et al.*, 2015 *Nucl. Fusion* **55** 043009.
- [24] Castaldo C. *et al.*, 2016 *Nucl. Fusion* **56** 016003.
- [25] Goniche M. *et al.*, *Edge plasma–lower hybrid wave interaction and current drive efficiency*, 42nd EPS conference, Lisbon, Portugal, 22-26 June, 2015
- [26] Cesario R. *et al.*, 2011, *Plasma Phys. Contr. Fusion* **53** 085011.
- [27] Wallace G. M. *et al.*, 2010 *Phys. Plasma* **17** 082508.
- [28] Barbato E. *et al.*, 2014 *Nucl. Fusion* **54** 123009
- [29] Ding B. J. *et al.*, 2013 *Nucl. Fusion* **53** 113027.
- [30] Cesario R., *et al.*, 2014 *Nucl. Fusion* **54** 043002.
- [31] Takase Y. and Porkolab M., 1983, *Phys. Fluids* **26** 2992.
- [32] Baek S. G. *et al.*, 2014, *Phys. Plasmas* **21**, 061511.

- [33]Porkolab M. 1977 *Phys. Fluids* **20** 2058.
- [34]Liu C.S. *et al.*, 1984 *Phys. Fluids* **27** 1709.
- [35]Mumgarrd B. *et al.*, 2015 *Bull. Am. Phys.* **60** CP12.019.
- [36]Decker J., *et al.*, 2014 *Phys. Plasmas* **21**, 092504.
- [37]Peysson Y. *et al.*, 2012 *Plasma Phys. Contr. Fusion* **54** 045003.
- [38]Peysson Y. *et al.*, 2008 Theory of fusion plasmas *AIP Conf. Proc.* **1069** 176.
- [39]Peysson Y. *et al.*, 2016 *Plasma Phys Contr. Fusion* **58** 044008.
- [40]Smirnov A. P., Harvey R., 1995, *Bulletin of the American Physical Society* **40** 1837.
- [41]Harvey R. W. and McCoyM., 1992, “The CQL3D Fokker-Planck Code”, in Proceedings of the IAEA Technical Committee Meeting on Simulation and Modeling of Thermonuclear Plasmas, 489-526
- [42]Shiraiwa S. *et al.*, 2015, *AIP Conf. Proc.* **1689** 030016.
- [43]Wallace G.M., *et al.*, 2012 *Phys. Plasmas* **19** 062505.
- [44]Kirov K. *et al.*, 2016, *Plasma Phys Contr. Fusion* **58**, 125001.
- [45]Kirov K. *et al.*, 2010 *Nucl. Fusion* **50** 075003.
- [46]Kirov K. *et al.*, 2012 *Plasma Phys Contr. Fusion* **54** 074003.
- [47]Nilsson E. *et al.*, 2013 *Nuclear Fusion* **53** 083018.
- [48]PeyssonY. and J. Decker J., 2014 *Fusion Science and Technology* **65**, 22-43.
- [49]Artaud J. F. *et al.*, 2010 *Nuclear Fusion* **50** 043001.
- [50]Goniche M. *et al.*, 16th Topical Conference on Radio Frequency Power in Plasmas (2005), *AIP Conf. Proc.* 787, pp. 307-310; doi: <http://dx.doi.org/10.1063/1.2098245>.
- [51]Poli F. M., *et al.*, 2016 *Plasma Phys Contr. Fusion* **58** 095001.